Icarus 441 (2025) 116690

Contents lists available at ScienceDirect

Icarus

journal homepage: www.elsevier.com/locate/icarus

Research Paper

# Transient and tidal wave precursors and atmospheric impacts of Mars' flushing storm initiated regional storms in reanalysis data

Márton Mester [a,*], R. John Wilson [b], Melinda A. Kahre [b]

[a] NASA Postdoctoral Program, NASA Ames Research Center, Moffett Field, 94035, CA, United States of America
[b] Space Science and Astrobiology Division, NASA Ames Research Center, Moffett Field, 94035, CA, United States of America

ARTICLE INFO

*Keywords:*
Mars
Atmosphere
Climate
Atmospheres
Dynamics
Meteorology

ABSTRACT

Regional dust storms develop in the Southern Hemisphere (SH) of Mars typically three times in years that do not experience a Global Dust Storm. The Thermal Emission Spectrometer and the Mars Climate Sounder instruments on board Mars Global Surveyor and Mars Reconnaissance Orbiter, respectively, have observed that the storms that generally appear in the $L_s = 210° - 240°$ and $L_s = 310° - 330°$ time periods, commonly referred to as A- and C-season regional dust storms, respectively, are preceded by atmospheric dust 'flushed' into the SH from the Northern Hemisphere (NH) mid-latitude storm track through one of the vast lowland channels, most frequently via Acidalia–Chryse or Utopia–Isidis. Here, reanalysis data are used to analyze the typical behavior of transient and tidal waves before and after cross-equator flushing storms that trigger regional storms, revealing the characteristic atmospheric wave evolution surrounding these events. In particular, the analysis shows that a strong wavenumber 3 transient wave and a mid-latitude tide amplification typically precede flushing events. Furthermore, our results suggest that while Acidalia-related regional storms typically require multiple high-amplitude wave events, regional storms initiated through Isidis may happen more abruptly.

## 1. Introduction

Atmospheric dust is one of the major driving components of the Mars climate. Airborne dust not only directly influences the thermal structure of the atmosphere, but there are also strong couplings between the dust, water, and $CO_2$ cycles (Kahre et al., 2017). Recent studies also reveal a coupling with the chlorine cycle via dust particles, providing a platform for heterogeneous processes (Taysum et al., 2024; Streeter et al., 2024b). Most of the variability in the dust cycle is due to dust storms that are regular events on Mars. These storms can be distinguished by size and classified as local, regional, or global dust storms (e.g. Martin and Zurek, 1993; Cantor et al., 2001). Although global dust storms occur once every approximately 3 Martian years (MYs), regional dust storms typically occur during three seasonal windows each year without a global dust storm. These seasons, named A, B, and C seasons by Kass et al. (2016), range from $L_s = 205° - 270°$, $245° - 295°$, and $305° - 335°$, respectively. Dust storms in the B season are confined to the south pole over the receding $CO_2$ ice cap (Kass et al., 2016) without altering the global circulation and are understood to be initiated by polar cap edge stresses (Batterson et al., 2023). Conversely, A and C season regional dust storms are observed to be preceded by 'flushing' storms (Wang et al., 2013) when dust is flushed down from the Northern Hemisphere (NH) to the Southern Hemisphere (SH) where the increased surface stresses initiate further, sudden dust lifting, eventually manifesting in a regional-scale storm encompassing a wide range of latitudes and longitudes. The increased dust loading accompanying regional storms in the A and C seasons leads to numerous changes in the general circulation, including the amplification of thermal tides (Wilson and Hamilton, 1996), strengthening the Hadley circulation, suppression of low-level transient wave activity (Battalio and Wang, 2020), and weakening of the NH polar vortex by reducing both its areal extent and ellipticity (Alsaeed et al., 2024; Streeter et al., 2024a). Therefore, the occurrence of regional dust storms in the A and C seasons is one of the most influential events in the lower atmosphere of Mars. As such, accurately forecasting these regional dust storms would be tremendously useful for future human settlements on Mars.

Flushing storms (first termed as such by Wang et al., 2003) were first observed in Mars Orbiter Camera (MOC) imagery onboard Mars Global Surveyor (MGS) in 1999 (Cantor et al., 2001) when dusty frontal structures were visible in the NH moving equatorward and were associated with transient (or baroclinic) wave structures. Since their discovery, flushing storms have attracted great attention in the Mars climate community (Wang and Richardson, 2015). However, it is not yet clear what conditions are needed for these frontal storms to develop

* Corresponding author.
*E-mail addresses:* marton.mester@nasa.gov (M. Mester), robert.j.wilson@nasa.gov (R.J. Wilson), melinda.a.kahre@nasa.gov (M.A. Kahre).

https://doi.org/10.1016/j.icarus.2025.116690
Received 11 December 2024; Received in revised form 30 May 2025; Accepted 4 June 2025
Available online 19 June 2025
0019-1035/© 2025 Elsevier Inc. All rights are reserved, including those for text and data mining, AI training, and similar technologies.

and propagate south to trigger regional storms. Although smaller, local dust storms have been seen to travel from NH to SH through Arcadia, observed regional storms were preceded by storms flushed through either Acidalia–Chryse or Utopia–Isidis. Although there is still no consensus on the conditions necessary for regional storm onset and the exact roles that flushing storms play, several advances have been made in the past two decades. Wang et al. (2003) have demonstrated using a Lagrangian particle transport model applied offline to Mars general circulation model (MGCM) output that cross-equator dust transport may be limited by a 'tidal gate', as synchronization between low-latitude tides (on the NH) and mid-latitude transient waves is necessary for the dust particles to penetrate to the South.

The characteristics of baroclinic waves have received increased attention due to their relevance to the onset of regional storms. Numerous studies have suggested that flushing storms tend to occur in seasons when the wavenumber 3, or wave-3, component of the baroclinic wave is strong and is, in fact, dominant, e.g., during $L_s = 220 - 238°$ (Hinson and Wang, 2010). This has been elucidated in detail for the case of the MY 24 Acidalia-type A-season storm and the MY 26 Utopia-type A-season storm using MOC imagery and Thermal Emission Spectrometer (TES) data (onboard MGS) (Wang et al., 2005) and later reconfirmed for the MY 24 A-season storm with reanalysis data (Wang, 2018). The increasing number of years of spacecraft monitoring has allowed for more extensive studies, including (Hinson and Wilson, 2021) spanning MY 24-33 TES and MCS (Mars Climate Sounder) data, showing that several regional storms were preceded by strong wave-3 activity and that the MY 31 Utopia-type A-season storm was preceded by a strong wave-2 responsible for flushing. They have also commented that MY 26 and MY 33 A-storms (also Utopia-type) had strong wave-2 activity. Furthermore, measurements collected by the Rover Environmental Monitoring Station (REMS) on the Curiosity Rover in Gale crater indicate that A-season regional storms are preceded by an amplification of transient waves in MYs 32, 33 and 35 (Zurita-Zurita et al., 2022).

It has been suggested that the seasonality of regional storms is driven by the seasonality of the wavenumber 2 and wavenumber 3 components of the transient waves, wave-2 being the dominant before $L_s = 220°$ and wave-3 being the dominant after that date (Hinson and Wilson, 2021). According to this suggestion, wave-2 is theorized to be responsible, on at least a few occasions, for Utopia-type storms, and wave-3 is responsible for Acidalia-type flushing. Therefore, one of the key precursors of flushing storms could be a strong wave-3 or wave-2 wave (depending on the season); however, the connection between high-amplitude events and flushing storm onsets is not yet identified in a unified approach, only via case-by-case inspection. It has also been suggested that the baroclinic annular mode, a combination of different wavenumbers thereby capturing both wave-2 and wave-3 evolution, of Mars can be a predictor of regional dust storms (Battalio and Lora, 2021).

Although there have been advances in understanding precursors and impacts of flushing storms, the event-by-event variability of these precursors and impacts has not yet been compactly analyzed and assessed. Although there seems to be a clear indication of wave-3 amplification before some flushing events, the typical time lag between the wave-3 spike and the flushing storm onset has not been categorized yet. Furthermore, differences between Acidalia-type and Utopia-type storms have not yet been documented in detail, and it is poorly understood how much influence wave-2 waves have on Utopia-type storms and if it is wave-2 or wave-3 that is more vital in regional storm initiation through Utopia. Although it has been suggested that tides may play a role in the initiation of flushing storms, very limited attempts have been made to identify precursors in the tide field.

Composite analysis, or conditional sampling, is a well-established, simple, but powerful statistical technique widely used in various scientific fields, including the Earth's magnetic field (Chree, 1913) and climate to identify potential predictors and impacts of various phenomena (Storch and Zwiers, 1999). The analysis is carried out by first identifying a set of events and then calculating the composite mean, i.e. averaging over all identified events either through an entire time period or with respect to the occurrence of a recurring event. By averaging through multiple events, atmospheric variability is reduced so that signals from the physical mechanisms linked to the recurring event are amplified. Given the increasing amount of observations and reanalysis data, now spanning more than a dozen regional dust storms, composite analysis has become a potentially suitable method to capture precursors and impacts shared across different regional storm events, with some limitations imposed by the still relatively low sample size.

In this study, we aim to characterize the precursors and impacts of A- and C-season regional dust storms in a compact and unified manner, establishing similarities and differences between A- and C-season regional storms and between Acidalia- and Isidis-type storms. To this end, we used the OpenMARS reanalysis dataset to apply a composite analysis of various atmospheric descriptors, including eddy and tide kinetic energy, transient temperature waves and temperature tides, dust opacity, and surface stresses. This paper is organized as follows. In Section 2, we discuss the datasets used, methodology, and regional storm categorization. Section 3 contains the results of the composite analysis. In Section 4, we discuss the results, and Section 5 provides conclusions.

## 2. Methods

This work uses reanalysis data (Section 2.1) to perform a composite analysis (Section 2.2) of A and C season regional dust storms, with the composited storms centered about their onset date (defined in Section 2.2.1). We will determine which MYs and seasons had no regional storms according to this onset definition and we will compare the determined regional storm onset dates with regional storms determined in previous studies (Section 2.2.2), including Battalio and Wang (2021), Hinson and Wilson (2024), Martín-Rubio et al. (2024). Furthermore, we examine the column dust optical depth evolution to determine whether a regional storm was triggered by a flushing event through Acidalia or Isidis, and we find discrepancies with earlier works in the cases of MY 32 and 33 A regional storms (Section 2.2.3). We classify each regional storm as Acidalia or Isidis-type and establish groups of regional storms based on temporal (i.e., A or C season) and spatial patterns (i.e., Acidalia or Isidis-type) (Section 2.2.4) to construct composites of regional storms of different types. Finally, we describe how we determine stationary, transient, and tidal waves (Section 2.3), to be used in the composite analysis.

### 2.1. Datasets

#### 2.1.1. OpenMars reanalysis dataset

We characterize flushing storm-initiated regional storm climatology primarily using the OpenMARS (Open access to Mars Assimilated Remote Soundings) reanalysis dataset, combining the Planetary Climate Model, UK spectral variant (PCM-UK), with atmospheric observations. The spectral model was run at 31 horizontal and 35 vertical levels, using observations from the Thermal Emission Spectrometer (TES) during MY 24–27 and Mars Climate Sounder (MCS) retrievals during MY 28–35. More details on the data set and the assimilation scheme can be found in Holmes et al. (2020). In this study, we use the velocity, temperature, and surface pressure from the reanalysis data set and the visible column dust optical depth field (vCDOD) adapted from Montabone et al. (2015). The vCDOD field is normalized to the reference pressure level of 610 Pa to account for topographic effects, and we use the normalized column dust optical depth CDOD = vCDOD $\times$ 610Pa/$p_s$ in our analysis, where $p_s$ is the surface pressure. The obtained CDOD field is used in this study to define regional storm onsets (Section 2.2.1) and to analyze the individual (Section 2.2.3) and composite (Sections 3.1.1, 3.2.1, 3.3.1, 3.3.2) tempo-spatial evolution of the atmosphere during and preceding regional storms. The velocity

and temperature data are used to determine the composite evolution of different modes of transient (or baroclinic) waves (Sections 3.1.2, 3.2.2, 3.3.3) and tides (Sections 3.1.3, 3.2.3, 3.3.4) during and preceding regional dust storms. It is expected that wave pulse events (of a given wavenumber) in temperature and wind strength will coincide, since at leading order thermal wind balance directly relates the amplitudes of the linearized temperature and wind perturbations. However, this proportionality is also impacted by the basic temperature profile and nonlinear effects, and direct proportionality is not expected between individual events when the atmospheric state is changed (e.g., by dust content). Furthermore, the meridional velocity field will be used to explore the 'Tidal Gate' theory (in Section 3.3.5), which we briefly introduce in Section 2.3.2.

#### 2.1.2. Comparison of baroclinic wave amplitude peaks in OpenMARS and MCS data

As highlighted by Greybush et al. (2019a), there is an apparent poor quality of assimilation results in both OpenMARS and EMARS with the MCS observations (as opposed to TES), and eddy field quality is compromised in both reanalyses, resulting in potential limitations to make use of the reanalyses to assess baroclinic waves. The limitation is evidently due to polar-hood aerosols preventing MCS from sounding the lower atmosphere at high northern latitudes in the winter season, as shown in Fig. 1 of Hinson and Wilson (2021). For this reason, the MCS profiles are not sufficient to produce a consistently reliable reanalysis of eddy activity near the surface in the northern hemisphere. Further spurious signals have been found in both OpenMARS and EMARS that are due to data gaps, data volume and quality changes, and spacecraft orbital aliasing (Battalio, 2022; Wang et al., 2024), potentially affecting any results based on these reanalysis products. These limitations of the reanalysis datasets may result in sporadic artificial signals (which can be substantial), contaminating the results. By applying a composite analysis (Section 2.2), we expect these signals to average out and reduce significantly, but systematic artificial signals will still remain. In order to test the reliability of OpenMARS in capturing baroclinic waves, we performed a brief comparison of transient (or baroclinic) waves in OpenMARS and MCS brightness temperature data. More precisely, we compared the low-level transient temperature waves (at approximately 1 km) in OpenMARS with MCS T32 brightness temperature eddies as described in Hinson and Wilson (2021). While there is a systematic failure of 3 am temperature retrievals at roughly 60N in the winter season and peaks at solstice (Greybush et al., 2019a; Hinson and Wilson, 2021), brightness temperatures do not suffer this limitation and offer observational data twice a day. While the two temperature fields are not directly comparable, it is possible to check if and when peaks in the temperature wave amplitudes align in time (Fig. 1). We found that until around $L_s = 220°$ the timing of wave-1 and wave-2 amplitude peaks in MCS and OpenMars align well. In particular, we see agreement across the two datasets regarding the timing of wave-1 peaks in MYs 30–33 occurring around $L_s = 210°$, the wave-1 peak at $L_s = 195°$ in MY 32, wave-2 peaks in MYs 30–32 around $L_s = 200 - 205°$, and in MY 29 around $L_s = 215°$. Neither the wave-1 and wave-2 temperature transient waves exhibit a solstitial pause in OpenMARS (unlike brightness temperature in MCS data); hence the reanalysis might not be reliable at all in the solstice season for assessing low-level transient waves. Additionally, in the $L_s = 240 - 320°$ season, the match between the datasets is poor. The exact timing when OpenMARS becomes more reliable again is not clear, but in the case of wave-1 and wave-2 it might only become reliable again late in the post-solstice season. A correlation in amplitude peaks for these waves only clearly emerges after $L_s = 340°$, including wave-1 amplitude peaks in MYs 30 and 31 around $L_s = 350°$. On the other hand, wave-3 seems to be better represented in OpenMARS as early as $L_s = 300°$, illustrated by the match in amplitude peaks, for example, in MY 30 at $L_s = 320°$ and 330°, and MY 32 at $L_s = 330°$. Overall, the comparison of OpenMARS temperature transient waves and MCS brightness temperatures suggests that OpenMARS qualitatively captures transient wave amplitude peak timings and trends until $L_s = 220 - 240°$ and after $L_s = 340°$. However, the wave-3 transient temperature field looks reliable as early as $L_s = 300°$. Keeping in mind these limitations, OpenMARS can be expected to capture the eddy fields during A season regional storms (with the earlier storms being represented more accurately) and at least the wave-3 eddy fields during C season regional storms.

#### 2.1.3. EMARS reanalysis dataset

Apart from OpenMARS, we also consider output from the Ensemble Mars Atmosphere Reanalysis System (EMARS) Version 1.0 Dataset (Greybush et al., 2019b), which, similarly to OpenMARS, uses observations from TES and MCS, however, differs in the underlying dynamical model (GFDL MGCM) and in the assimilation scheme, and covers only the shorter MY 24–32 period compared to OpenMARS. Although we use OpenMARS for most of our analysis, we use EMARS reanalysis data to confirm that our key findings from the composite analysis are present in both reanalyses, i.e., the findings are not artifacts of the reanalysis assimilation method itself. In addition, EMARS contains assimilated surface stress reanalysis data that we include in our treatment.

### 2.2. Composite analysis

We performed a composite analysis to assess the typical state of the atmosphere before flushing storms and after the onset of regional storms. We consider composites of different fields, such as CDOD or temperature, for regional storms that we will have identified. A composite of a scalar field $\Phi(\boldsymbol{x}, t)$ is typically constructed by averaging over all regional storms while taking the time relative to the onset date, i.e., the composite field $C$ of $\Phi$ is given by

$$C(\boldsymbol{x}, t) = \frac{1}{N} \sum_{k=1}^{N} \Phi(\boldsymbol{x}, t_k + t), \tag{1}$$

where $t_1, t_2, \ldots, t_N$ are the regional storm onset dates. In this study we consider $(-30 < t < 30)$ sol composites.

Since there were no TES or MCS observations in MY 27, and MCS had retrieval issues in MY 28, we did not include these years in our study. Furthermore, MYs 25 and 34 had a global dust storm that started in the $L_s = 180° - 190°$ season before the A season. Consequently, in these years, no regional storms began during the A-season. Hence, we restrict our attention to considering SH dust storms in the A and C seasons in MY $24, 26, 29, 30, 31, 32, 33, 35$ with additional MY 25,34 for C seasons only, and we associate time windows $L_s = 200° - 245°$ with the A season and $L_s = 290° - 335°$ with the C season.

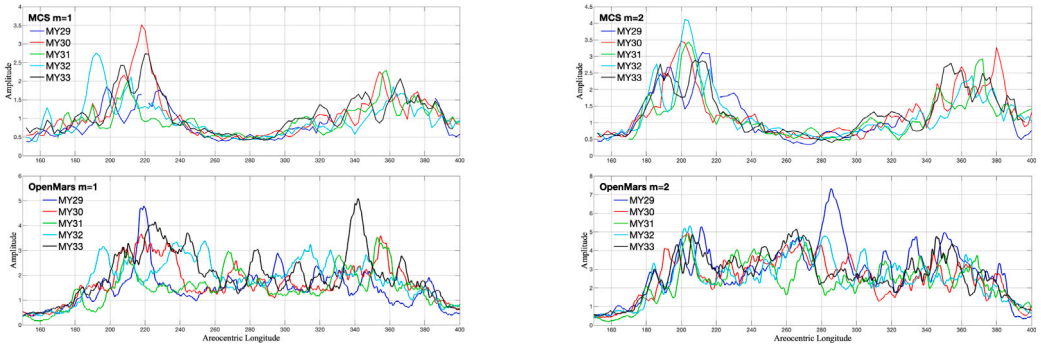
Composite analysis requires a definition of the onset of regional storms guided by intuition but sufficiently objective to determine regional storms consistently in an automated manner. Here, we focus on when the storm from NH has already reached the SH and started the onset of sudden dust lifting. Consequently, our onset date does not correspond to when the flushing occurs through the equator but shortly after when the dust is lifted abruptly in the SH. Hence, our onset date can be interpreted as a 'regional storm onset date' rather than a 'flushing storm onset date.' Our definition successfully captures the year-by-year evolution of the regional dust storms and the preceding flushing storms consistently, allowing the exploration of the typical behavior of the different atmospheric structures (e.g., transient and tidal waves) before and after onset.

#### 2.2.1. Regional storm onset definition

Our definition of the onset of regional storms is primarily motivated by capturing the intensification of the localized dust lifting accompanying the formation of regional storms. As highlighted in the literature (e.g., Hinson and Wilson, 2024), the localization of dust lifting projects in various wave modes of the CDOD field, most prominently on wavenumber-1. Similarly, an abrupt increase in the

(a) Comparison of wave-1 amplitude temperature waves.

(b) Comparison of wave-2 amplitude temperature waves.




(c) Comparison of wave-3 amplitude temperature waves.

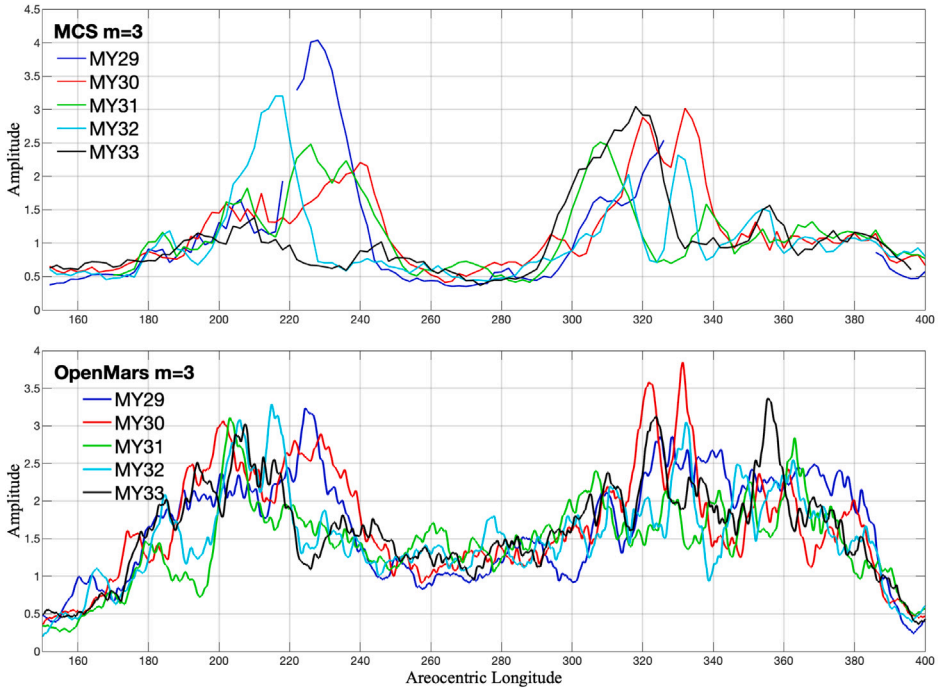



**Fig. 1.** Comparison of low-level transient waves in OpenMARS with brightness temperatures from MCS data.

amplitude of the wave-1 component of CDOD may be related to localized dust lifting. Consequent sustained and/or slowly weakened wave-1 amplitudes can result from further localized dust lifting, advection of the dust cloud, or a combination of both. Consequently, in each A and C season time window, we calculate the time evolution of the zonal wavenumber-1 amplitude $D_1(\theta, t)$ of the CDOD field, where $\theta$ denotes latitude. For each season, at each reanalysis time step, we calculate the maximum $M_1(t)$ of the wavenumber-1 amplitude in the latitude band 2.5°S–32.5°S, i.e.

$$M_1(t) = \max_{\theta \in (2.5°S - 32.5°S)} D_1(\theta, t). \tag{2}$$

Next, we separately calculate the mean $\mu_M$ and standard deviation $\sigma_M$ of $M_1(t)$ in the different years and storm seasons. We identify a *potential* regional storm onset date in a (A or C) storm season when $M_1(t)$ exceeds $M_{crit} = \mu_M + 2\sigma_M$ the first time in the storm season. Here, we decide against the possibility of including two regional storms in a given storm season (e.g., in MY 32 C) as the ongoing impacts of the previous storm arguably compromise the precursors of the second storm. Since the mean and standard deviation were calculated separately for the different storm seasons, the $M_{crit}$ value changes for different MYs and seasons. The main reason we propose such a definition is that in other years, regional storms can take place at different background dust distributions. We find that a unified, fixed threshold for the wave-1 amplitude could either ignore regional storms in some years (if this threshold is too high) and could identify non-events as regional storms (if the threshold is too low). As shown on Table 1, the value of the amplitude threshold $M_{crit}$ may differ significantly in different seasons and MYs.

This definition needs some refinement, as in a weak, non-dusty season, the two-standard deviation limit could be exceeded without a storm. Therefore, we also require that the zonal mean of the dust opacity field in the 2.5°S–32.5°S latitude band exceeds 0.9 at some latitude within five sols of the potential onset date (either pre- or post-). If both the wavenumber-1 (CDOD) condition and the zonal mean

**Table 1**
Regional storm onset criterion thresholds and onset dates based on our proposed definition. The corresponding storms identified by BW21 for MYs 24–31 (MYs covered by BW21). Onset dates provided by HW24 and MR24 (based on temperature or CDOD) are also included. While our analysis determines a regional storm in MY 32 C-season, we exclude it from our composites as it was initiated at the SH.

| MY | season | $\mu_M$ | $\sigma_M$ | $M_{crit}$ | $L_s$ | BW21 classification | HW24 | MR24: T/CDOD |
|---|---|---|---|---|---|---|---|---|
| 24 | A | 0.09 | 0.10 | 0.30 | 225 | m08-1 Turning (Acidalia), m08-3 Flushing (Acidalia) | 223 | 225/225 |
| 26 | A | 0.12 | 0.17 | 0.45 | 214 | r06-2 Flushing (Utopia) | 210 | 215/220 |
| 26 | C | 0.15 | 0.25 | 0.65 | 315 | r12-2 Turning (Acidalia) | 314 | 316/315 |
| 29 | A | 0.16 | 0.21 | 0.59 | 235 | B07-2 Flushing (Acidalia) | | 222/225 |
| 29 | C | 0.10 | 0.13 | 0.36 | 310 | B11-1 Flushing (Utopia) | | 310/315 |
| 30 | A | 0.08 | 0.07 | 0.21 | 232 | G07-3 Flushing (Acidalia) | | 232/240 |
| 31 | A | 0.21 | 0.33 | 0.87 | 208 | D06-1 Flushing (Utopia) | 207 | 208/210 |
| 31 | C | 0.16 | 0.26 | 0.69 | 313 | D11-3 Turning (Acidalia) | 309 | 312/315 |
| 32 | A | 0.18 | 0.25 | 0.69 | 219 | | 218 | 218/215 |
| 32 | C (excl.) | 0.12 | 0.18 | 0.48 | 317 | | | 311/310 |
| 33 | A | 0.15 | 0.20 | 0.55 | 216 | | | 218/225 |
| 33 | C | 0.25 | 0.32 | 0.89 | 322 | | | 325/320 |
| 34 | C | 0.23 | 0.41 | 1.06 | 320 | | 319 | 320/320 |
| 35 | A | 0.10 | 0.14 | 0.38 | 229 | | 225 | 225/225 |
| 35 | C | 0.17 | 0.29 | 0.74 | 315 | | 313 | 315/315 |

(CDOD) condition are satisfied, we identify a regional storm (with the central date being the date when the wavenumber-1 amplitude condition is satisfied).

Our definition, therefore, corresponds to the date on which the southern hemisphere experiences a rise in wave-1 dust, which is understood to be a localized dust lifting in the south. Therefore, a potential flushing through the equator and the generating mechanism (to be considered later in this paper) occurs earlier. We would also like to point out that our definition might not (and actually will not) always correspond to a flushing storm-initiated regional storm, as our definition captures dust lifting in the south but not necessarily cross-equator initiation.

In particular, the MY 32 C-season regional storm we identified was preceded by strong SH cap edge dust storms activity high latitudes. These SH storms were on a decline by the time the regional storm onset occurred, and it is not definitive whether these cap edge dust storms were responsible for the regional storm initiation. Hence, the MY 32 C-season regional storm is discarded from our composites. Although there was arguably a second regional storm of the C season in MY 32, the impacts of the first regional storm compromise the inclusion of the second storm of the MY 32 into the composite, and hence we exclude the C season in MY 32 entirely from our analysis.

#### 2.2.2. Non-flushing seasons and previous storm onset classifications

Our regional storm onset managed to capture regional storms in each of the years and seasons investigated, except the C seasons in MY 24, 25, and 30. Although the MY 30 A-season storm is a characteristically weak storm, it did pass our definition thresholds. The onset dates are shown in Table 1, where we also refer to the dust storms identified from MOC and MARCI (Mars Color Imager, onboard MRO) images by Battalio and Wang (2021, BW21 hereafter, available until MY 31) at that solar longitude. We would like to highlight that BW21 also did not identify a regional storm in the C season of MY 24 and 25. However, they did find a MY 30 C-season dust storm that did not satisfy our definition. We also include onset dates from Hinson and Wilson (2024, HW24 hereafter) for comparison, who listed five A and five C season regional storms and determined the onset date by visual inspection of CDOD zonal asymmetries with 1–2 sol uncertainty according to their estimates. The onset dates proposed by Martín-Rubio et al. (2024, MR24 hereafter) are also included, who studied interannual variability and identified an onset date when the zonal mean temperature at 50 Pa and the zonal mean dust opacity exceeded the thresholds of 200 K and 0.3, respectively (at some latitude), using retrievals from TES and MCS.

The onset dates are generally in good agreement between different definitions; however, a few outliers clearly show differences. In the A-season of MY 29 the NH dust levels were already high before the flushing and the regional storm onset in the SH, so MR24 finds an earlier onset date. Furthermore, the MY 32 C-season regional storm was arguably not triggered by flushing, but it was initiated at the SH subpolar latitudes; the MR24 definition captures this as their onset condition is satisfied at high SH latitudes well before our definition is satisfied. These differences highlight that specifying a dust storm onset definition is a subtle act and may depend on what the definition aims to capture. Here, we apply our definition with the aim of capturing the time when vigorous dust lifting at the SH has been initiated and the strongly localized dust plume has appeared. A further difference between the proposed definition and MR24 is the value of CDOD used. While their value is much lower, it is due to their approach in which they identify the duration of the entire storm when the CDOD exceeds 0.3, and the determination of the onset date is not their main objective.

#### 2.2.3. Categorization of the MY 32 and 33 A-season regional dust storms

One of the objectives of this study is to establish similarities and differences between regional storms triggered by different flushing channels. To determine which regional storms were triggered by Acidalia flushing or Isidis, we inspected the spatial evolution of CDOD for individual regional storms; we have determined alternative classifications to previous classifications of the regional storms in the A seasons of MY 32 and 33.

The MY 32 A-season regional storm has been argued to have been triggered first by dust-lifting activity in Hellas and then reinforced by flushing through Acidalia (Wang et al., 2023). This view has been adapted by different studies since then (e.g. Hinson and Wilson, 2024). Based on MARCI imagery, Wang et al. (2023) showed that Acidalia experienced high dust activity prior to $L_s = 220°$. More specifically, several sequences of flushing storms between $L_s = 200-220°$ preceded the regional storm, first in Utopia–Isidis and subsequently in both Acidalia–Chryse and Arcadia-Amazonis (Wang et al., 2023, Fig. 4). Hence, all three channels were active prior to the regional storm onset. However, the 'storm sequence' images (Fig. 9 in Wang et al. (2023)) do not reveal any regional storms that were triggered by flushing through Acidalia. Instead, they recognized two distinct storm sequences, one of which originated in Hellas and one in Utopia. They argued that the Hellas storm and Acidalia activity would merge and result in a regional storm; however, they did not picture the Utopia storm (which they determined to occur almost simultaneously with the Hellas storm). The Utopia storm was not fully captured by MARCI, as key images were not taken at the right times, hence it cannot be ruled out that a possible Utopia flushing sequence triggered the Hellas storm. Given our goal to identify preconditions for regional storm onset, it could be misleading to refer to the 32 A-season regional storm as an Acidalia storm since (whether the Utopia activity was influential or not) its initiation seems to be linked to Hellas (and/or Isidis-Utopia). In our assessment, we find that the

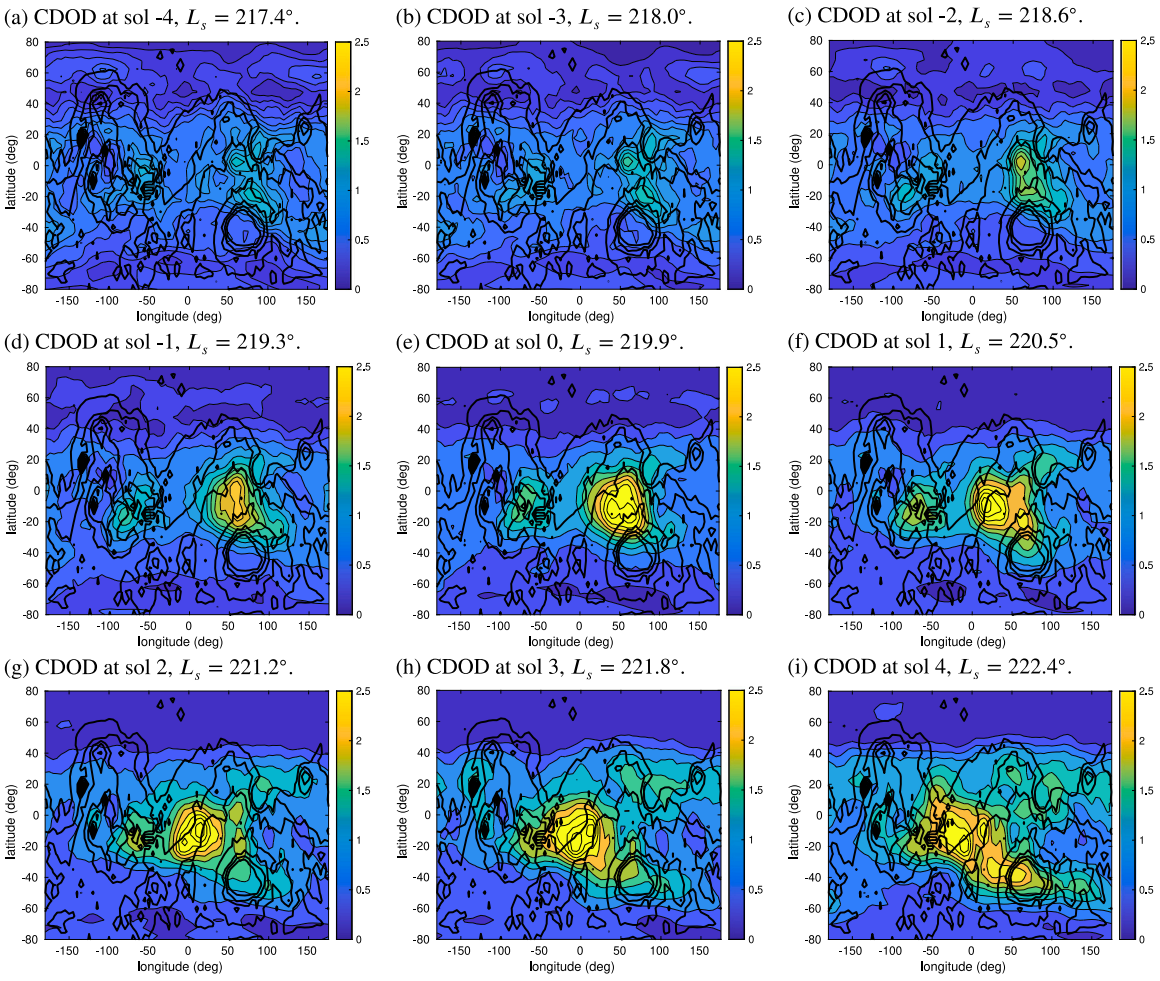



**Fig. 2.** Daily CDOD snapshots between sol −4 and sol 4 (a-i) for the MY 32 A-season regional dust storm.

OpenMARS data (and consequently the dust climatology of Montabone et al. (2014) as well) suggest that there is a stronger link between the regional storm and Isidis than described by Wang et al. (2023). Fig. 2 shows a slight dust anomaly present at Isidis through the northern parts of Hellas at sol −4. At sol −2, an increase in dust is present, starting just west of Isidis at Syrtis Major. The dust storm then intensifies in the region between Hellas and Isidis. However, a clear dust anomaly is present south of Acidalia, which is not nearly as strong as the storm south of Isidis. The strong dust storm from the Isidis–Hellas region starts propagating to the west, and it is arguably regional scale by the time it merges with the moderate Acidalia storm during sols 2–4. Therefore, at least in OpenMARS data, the evolution of the CDOD suggests that the MY 32 A regional dust storm is not initiated by Acidalia-type flushing but is more likely a result of Isidis-driven initiation. It should be noted that the temporal reconstruction of the evolving CDOD field on such fine temporal scales is not necessarily accurate. The CDOD fields that are derived by Montabone et al. (2014) and drive OpenMARS are interpolated quantities from infrared dust opacity data that generally has large gaps in longitudes (about 30 degrees) each sol, and additional extrapolation errors are due to missing values in the bottom scale height. With our reclassification we do not mean to claim that the Acidalia/Hellas classification of Wang et al. (2023) was incorrect. Their classification was based on the observation that the regional storm peaked once the Acidalia and Hellas storm sequences merged. However, our results indicate that for the purposes of determining precursors, reclassification of the MY 32 A regional storm as Isidis-driven is more meaningful.

The MY 33 A-season regional storm has also been suggested to be a combined effort of Acidalia and Hellas (Wang et al., 2023). According to their analysis, Utopia dust activity ceased before the dust spike near Hellas and, consequently, was independent. In our investigation, similar to MY 32, we see closer links to Isidis than reported by Wang et al. (2023). Fig. 3 shows that the dust anomaly west of Isidis strengthens at sol −1, peaking at the beginning and then being advected to the west. Although there seems to be some activity south of Acidalia, OpenMARS data suggest that the onset of the MY 33 A-season regional dust storm is more closely related to Isidis. Consequently, in this paper, for the purposes of determining precursors, we categorize the MY 32 and 33 A-season regional storms as Isidis storms.

#### *2.2.4. Seasonal and spatial grouping of regional dust storms in composite analysis*

While we expect composites consisting of all regional storms to provide information on characteristics shared between all regional storms, there are significant seasonal differences in the climatology between the A- and C-seasons, and potentially key differences between storms Acidalia- and Utopia/Isidis-type storms. The regional storms in MY 32 and 33 A show a clear link with Isidis through CDOD snapshots, but past studies did not determine accompanying flushing storms through Utopia. We therefore categorize these storms as Isidis-type rather than Utopia-type in the rest of the paper.

In order to account for seasonal differences between A- and C-season storms and spatial differences between storms initiated by perceived flushing through different channels, we consider multiple composites based on seasonal and spatial properties of the different regional storms. Namely, we consider composites of

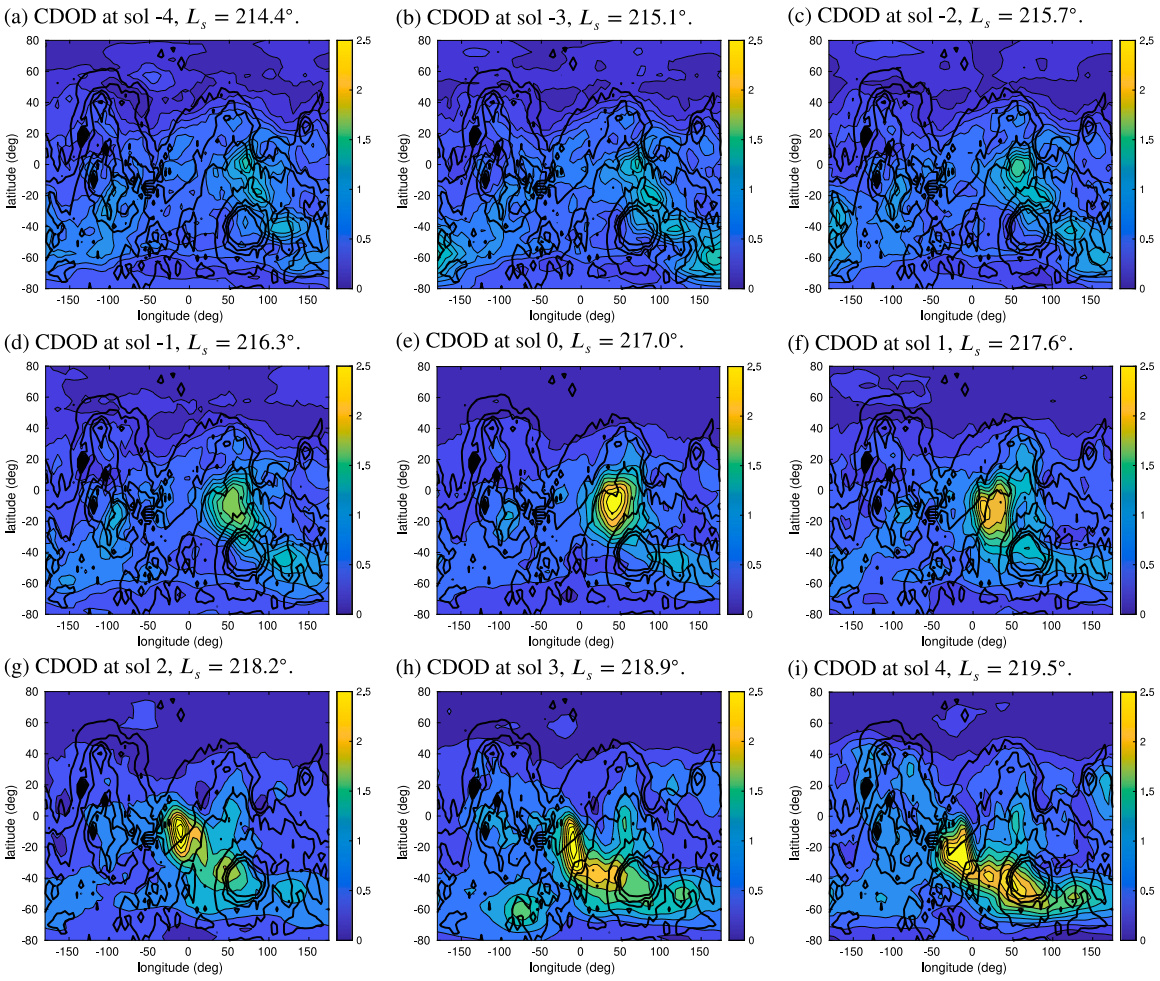



**Fig. 3.** Daily CDOD snapshots between sol −4 and sol 4 (a-i) for the MY 33 A-season regional dust storm.

1. all identified regional storms (14 storms),
2. all identified A-season regional storms (8 storms, MYs 24, 26, 29, 30, 31, 32, 33, 35),
3. all identified C-season regional storms (6 storms, MYs 26, 29, 31, 33, 34, 35),
4. A-season regional storms that are preceded by flushing through the Acidalia–Chryse channel (4 storms, MYs 24, 29, 30, 35),
5. A-season regional storms that are initiated through the Isidis (4 storms, MYs 26, 31, 32, 33).

Based on our classification of regional storms, it is worth noting that all Acidalia-related A season regional storms have onset dates on or after $L_s = 225°$, however, all Isidis-related A season regional storms have onset dates preceding $L_s = 220°$ (see Table 1).

### 2.3. Decomposition into tides, transient waves, and quasi-stationary waves

Atmospheric waves on Mars are typically categorized as either (thermal) tides, transient, or quasi-stationary waves (Barnes et al., 2017). Tides are excited by solar forcing and have periods that are unit fractions of a sol, with the diurnal (i.e., 1 sol period) and semi-diurnal (0.5 sol period) tides being the most dominant (Wilson and Hamilton, 1996). Transient waves here are referred to as waves with periods of a few sols (i.e., between 1.5 and 9.5 sols, Barnes et al. 1993). These waves on Mars are mostly understood to be of baroclinic origin, however barotropic wave growth (and suppression) can also contribute to their life cycle. Nonetheless, the waves we are referring to as transient waves are commonly referred to in literature simply as baroclinic waves. It is established that in Mars' lower atmosphere, a Fourier decomposition of transient baroclinic waves results in wavenumber 1, 2, 3 waves dominating, with periods approximately 6, 4, 2 sols, respectively (Hinson and Wilson, 2021). Quasi-stationary waves here represent waves with periods of more than 10 sols and can be part of the seasonal cycle or be initiated by inertial instability.

Since the periods of the different wave types are well separated, we identify the tide, transient, and quasi-stationary components of a field $v(t)$ by applying a 1-sol and a 10-sol running mean filter to calculate $v_1(t)$ and $v_{10}(t)$. The tide, transient, and quasi-stationary components of $v$ are given by $v_{tide}(t) = v(t) - v_1(t)$, $v'(t) = v_1(t) - v_{10}(t)$, and $v^*(t) = v_{10}(t)$, respectively. Then, we apply Fourier wave decomposition to determine transient waves of different spatial wavenumbers 1–3.

#### 2.3.1. Tide analysis

We further decompose the tide signal $v_{tide}$ by frequency and zonal wavenumbers and consider both eastward and westward propagating diurnal, semi-diurnal and ter-diurnal tides (that are waves with periods 24 h, 12 h and 8 h, respectively) with zonal wavenumbers 1–4 in this paper. We refer to the tide modes according to typical tide theory nomenclature, assigning three-character codes to the different modes describing frequency (D, S, $T$ for diurnal, semi-diurnal, ter-diurnal, respectively), propagation (W, E for westward or eastward) and zonal wavenumber, with the eastward propagating tides are typically associated with topographic modulation (Zurek, 1976; Forbes et al., 2002). The tide mode decomposition is done by double Fourier-decomposition of diurnal temperature variations, as typical in literature (see e.g., Wilson and Hamilton, 1996).

#### 2.3.2. Tidal gate theory

We will revisit in this study the 'Tidal Gate' theory introduced by Wang et al. (2003). The low-level meridional wind field is dominated by transient (baroclinic waves) at mid-latitudes and by tides at low-latitudes; hence, the possibility for cross-equatorial (from NH to SH) transport requires the near-equatorial tides to be southward, which happens between specific hours of local time. Outside of this time window, the 'Tidal Gate' is shut, and no NH-SH cross-equatorial transport is possible by advection. This suggests that the most efficient cross-equatorial transport is possible at a given latitudinal corridor if the mid-latitude transient meridional winds are equatorward between latitudes 20–40N during the earlier hours when the Tidal Gate is open. We will explore when and how well this condition is satisfied preceding regional storms in Section 3.3.5.

## 3. Results

We analyze composites of different subgroups of regional storms (provided in Section 2.2.4). In each subgroup, we analyze the zonal mean and wave-1 amplitude of CDOD, as well as the amplitudes of waves 1, 2 and 3 in the transient waves (in the temperature and wind fields) and a selection of tide modes, all derived from OpenMARS reanalysis data. First, we will consider the group of all determined (A and C season) regional dust storms, irrespective of season and location (Section 3.1). Then, we will consider separate composites to distinguish between A- and C-season regional storms, identifying shared traits and differences between the two seasons (Section 3.2). Next, we will compare composites of Acidalia- and Isidis-type A-season regional storms (Section 3.3). Furthermore, we revisit the 'tidal gate theory' (Wang et al., 2003) in Section 3.3.5 to extend our analysis on tide-transient wave interaction. We provide a brief comparison with EMARS in Section 3.4, which we use to elaborate on surface stress patterns surrounding regional storms (Section 3.5).

### 3.1. All regional storms

By considering composites of all regional storms that we determined and listed on Table 1, it is expected that properties typical to only one spatial (i.e., Acidalia or Isidis) or seasonal (i.e., A or C season) type will be less pronounced. However, properties that are characteristic of regional storms of any type are expected to be revealed more clearly by considering composites of all regional storms.

#### 3.1.1. Column dust optical depth

First, we consider the climatology of the CDOD surrounding the onset of the regional storm. We calculate the zonal mean and the amplitude of the wavenumber-1 component of CDOD to assess the composite evolution of dust (Fig. 4). The wavenumber-1 component reveals a localized dust-lifting in the SH that reaches its maximum within 3-4 sols after onset, then starts to decrease rapidly, persisting for approximately 10 sols. The wave-1 dust evolution could be explained by the fact that there is potentially a finite dust reservoir at the scene of the localized dust-lifting, which is drained completely in a few sols. Alternatively, the surface stresses can be weakened below a dust lifting threshold without exhausting all the dust available. Furthermore, the wave-1 event may not purely correspond to continuous dust lifting, but the localized dust cloud itself contributes to the wave-1 component (since the localized dust cloud projects on various wavenumber components of CDOD) of the dust field until it disperses within a few sols.

The high zonal mean CDOD levels are longer lived. The composite captures that once the dust is lifted, it is transported to the NH by the Hadley circulation, where high dust levels persist for at least 20–30 sols. The highest levels of dust opacity are initially located in the latitude band where dust lifting occurs, and decrease at higher northern latitudes. By sols 20–25, the moderate dust levels are balanced between 20N and 60S. Preceding onset, the composite suggests that the near-equator region has gradually increasing dust levels, already present between sol -20 and sol −10. However, this feature, as shown later, is a characteristic of A-season storms, particularly of Acidalia-type storms, and is not observed preceding C-season storms.

#### 3.1.2. Transient waves

We evaluated the evolution of transient waves by considering composites of the approximately 1 km above ground level (agl) temperature, meridional wind (or v field) and eddy kinetic energy (EKE) fields, here defined as

$$EKE = (u'^2 + v'^2)/2. \quad (3)$$

At mid-latitudes, the temperature composites (Fig. 5) reveal a generally weakening trend (calculated at each time as the maximum amplitude on the latitude band 37.5–62.5N, Fig. 5(d) in the amplitude of the wave-1, -2 temperature eddies. However, it shows a sharp peak in the wave-3 amplitude approximately 8 sols before and 0-1 sol after regional storm onset. Around onset, the wave-1 and wave-2 temperature amplitudes weaken, with wave 2 weakening starting few sols preceding onset and wave 1 weakening occurring about 15 sols after onset. Apart from the mid-latitudes, we can also see temperature wave-1, 2, 3 anomalies at low latitudes in the SH in the composites around the onset date. The peaks in the different wave mode amplitudes are present in the composites at every vertical level between the lowest model level and 6–8 km agl (not shown).

The meridional wind (not shown) and the EKE composites (Fig. 6(a)) also exhibit two peaks in wave-3 evolution around the same time as the temperature composite. We found that the wave-1 component of EKE is amplified towards the pole and does not attain its maximum at the mid-latitudes, leading to inconsistency between the wave-1 structure of temperature and EKE in the reanalysis. Since it is not sure whether this inconsistency is realistic or OpenMARS artifact, we disregard wave-1 component of EKE here and consider only wave-2 and wave-3.

Although the wave-2 EKE composite shows a weakening before onset (similarly to temperature), one may argue that it experiences a local peak after onset (Fig. 6(b)). The two peaks in the wave-3 fields do not necessarily mean that a regional storm is associated with two peaks. Instead, it is possible that some regional storms were preceded by wave-3 and some were accompanied by a wave-3 anomaly shortly after the SH dust lifting occurred. However, in the transient wave structure, the mid-latitude wave-3 peak of 8 sols before onset seems to be the most potent precursor, and a sharp weakening of wave-3 6–10 sols after onset is a consistent impact.

#### 3.1.3. Tide composites

Next, we are considering composites of temperature tides at 1 km agl. We have identified four different signatures in the tide composites that are present for various tide modes, and in Fig. 7 we show composites of tide modes DW1, DE1, DE3, SW2, SW3, TE2 to illustrate the identified signatures:

1. **Tide property 1 (TP1)**: Strengthening post-onset at 20–60S between sol 0 and 10 (see panels (a-e) on Fig. 7). This behavior is a signature of W modes, as is observed for all W modes apart from TW1 and is seemingly absent for E modes apart from DE1, DE2.
2. **Tide property 2 (TP2)**: Weakening post-onset at 40–60N between sol 0 and 10, a general feature of tides, as the trend is observed for all modes, apart from SW modes.
3. **Tide property 3 (TP3)**: Strengthening before onset at 40–60N (panels (a-c, e) in Fig. 7). Apparently, a characteristic property of wavenumber-3 and -4 waves, observed for both W and E for each of D, S, $T$ with potentially SW4 as an exception. This trend is also observed for DW1, DE1 and SE2.

4. **Tide property 4 (TP4)**: Weakening trend preceding onset, during sol −30 and 0 at 40–60N (panel (f) on Fig. 7). This behavior is observed for wave-2 diurnal and wave-1,-2 ter-diurnal tides (both W and E) DW2, DE2, TW1, TW2, TE1, TE2.

We can point out that TP2 and TP3 are signatures that were also seen in the composites of wave-3 eddies at mid-latitudes in Fig. 5. However, TP2 is observed for the majority of tide modes at various wavenumbers. This suggests that post-onset high-frequency (period less than 2 sols) mid-latitude waves are strongly suppressed. On the other hand, TP3 is primarily a feature of wave modes 3 and 4. Similarly, TP4 has been previously observed for wave-1 and -2 eddies (Fig. 5), suggesting that a mid-latitude weakening is more related to zonal wavenumber rather than to the temporal period. Finally, TP1 is barely observable for eddies; however, it is a clear feature of tides. Since the increase in the amplitude of the peak is closely aligned with the peak in the CDOD, TP1 can be explained by responding strongly to the evolving spatial distribution of dust-induced heating (Wilson, 2012).

Apart from the general signatures (TP1-4), which are shared across a wide range of tide modes, we also note that the strongest E amplitude in the composites is associated with DE3. Additionally, E modes with different frequency, but identical spatial wavenumbers show very similar behavior across time and space, with a weakening in amplitude at waves with higher frequency. A notable exception to this is the behavior of DE1 between 20–40N, where a distinct peak is observable at all times. Moreover, TW3 also expresses wave amplitudes in the 20–40N latitude band that are not present in other waves with wavenumber 3. This suggests that this characteristic of the tide in the composite is due to the topographic modulation of wavenumber 2 of DW1 (Forbes et al., 2002).

In order to discuss how much of these trends are seasonality and how much are actually impacts and precursors of regional storms, we need to distinguish between A- and C- seasons.

### 3.2. A- and C- season regional storms

#### 3.2.1. Differences in CDOD composites

By constructing separate composites of A and C storms, it is revealed (Fig. 8) that the wave-1 dust event in the SH after the onset date has similar lifetime (i.e., a weakening to climatological levels between lag 15–20 sols) for A and C storms; however, the A storm wave-1 events are peaking around 20S and then propagating to the south, whereas the C storm wave-1 events are peaking between 40S and 60S. The difference in spatial distribution suggests that the typical location of the dust lifting is different. However, a moderate wave-1 anomaly is present until sol 30 in the C storm composite, suggesting that the concentrated dust cloud is more coherent for longer than during A storms. The composites of the zonal mean dust opacity reveal multiple differences in the evolution of the dust field. At mid-latitudes in the SH, the high dust levels appear to last approximately 10 sols longer during A-storms than during C-storms. However, at low latitudes in the NH, dust opacity levels reach higher values during A storms and persist for much longer. The low latitudes in the NH experience a high dust content for more than 30 sols in the A seasons, whereas in the C seasons, dust is barely present after 20 sols. Seasonal differences in the Hadley circulation can explain the difference between A and C storms. The weaker C-season Hadley cell transports less dust to the NH, and the weaker winds allow the dust to settle on the surface more quickly.

#### 3.2.2. Transient waves

The A- and C-season composites of wave-1 and wave-2 transient temperature eddies share similarities (not shown) with the composites involving all storms, showing a weakening trend in both wave-1 and wave-2 amplitudes in both A- and C-seasons before and after onset. Furthermore, both the A- and C-season wave-3 composites show trends similar to the one revealed by the composite comprising all storms. Therefore, the composites suggest that the trend of temperature transient waves preceding and following regional storm onsets is similar for regional storms of the A and C seasons.

#### 3.2.3. Tide differences

The tide composites reveal more differences between the A and C seasons, particularly due to their distinct seasonal evolution. Since the two storm seasons are on different sides of the solstice, the subsolar point migrates in opposite meridional directions (southward in the A-season and northward in the C-season), resulting in a seasonal weakening/strengthening in the mid-latitude tides in the A-/C-season. The composite, which included both seasons (shown in Fig. 7) averaged these trends. However, these trends are clearly visible in the separate composites (see DW1 in Fig. 9). Although there is a strengthening trend in the C season, the tide amplification at NH mid-latitudes between sol −10 and 0 is anomalous. A slight weakening follows between sols 0 and 10, and the tide recovers its seasonality by sol 30. However, the tide seems to be stronger than seasonality at NH mid-latitudes between sol −20 and 0 in the A-season composite and then barely changes after onset. Mode DE3 expresses clear peaks between sol −10 and 0 for dust storms in the A- and C seasons (Fig. 9), suggesting that the wave-3 tide is a legitimate precursor for both storm seasons to predict regional storms.

Three key trends (TP1-3) identified in the composites comprising all storms are relatively robust; the mid-latitude trends, stronger tides between sol −10 and 0 (TP3), and weakening between 0 and 10 (TP2) are present for both A- and C-season storms. However, TP1 (regarding strong tides at 0–60S after onset) lasts for a shorter period of 10–20 sols during C storms before the tides recover their seasonal strengths. However, TP4 is dominated by A storms that occur when wave-2 eddies are seasonally weakening compared to C storms that occur at times when wave-2 amplitudes are relatively stagnant (Fig. 9).

### 3.3. Comparison of Acidalia–Chryse a storms and Utopia–Isidis a storms

#### 3.3.1. Differences in CDOD composites

The distinction between Acidalia–Chryse and Utopia–Isidis storms has resulted in significant differences in the zonal mean CDOD composites. It is apparent (Fig. 10) that while Acidalia storms are preceded by a more extended period of relatively high dust opacity at northern low latitudes, the state of the atmosphere before Isidis-type storms is much lower in dust content. Acidalia-type regional storms require sustained preconditioning, gradually increasing atmospheric dust content until a regional storm is initiated by additional sudden dust lifting. In contrast, Isidis events seem to be preceded by a slight rise in dust content at NH low latitudes approximately eight sols before onset, followed by a more abrupt onset that requires far less preconditioning than Acidalia storms.

The impacts of Isidis storms are also visibly distinct from those of Acidalia storms. Specifically, Isidis storms have seemingly more substantial effects in the SH between 20S–60S, lasting about 20 sols, with a relatively weak impact on the NH, with the highest dust concentrations lasting only approximately ten sols between 0–40N, and the high dust content is constrained to the 0–20N latitude band. The low impact on the NH could result from seasonality, as Isidis-type storms occur before $L_s = 220°$ when the Hadley circulation is relatively weak. In contrast to these features, Acidalia-type storms have more impact in the NH, with high dust levels present for more than 30 sols between 0–40N. Their effect on the SH is similar in duration to that of Isidis storms, albeit slightly weaker. Therefore, the composite analysis reveals qualitative differences between Acidalia and Isidis storms in terms of precursors and impacts in the CDOD field.

The wave-1 CDOD composites show similar trends in terms of tempo-spatial structure for the two different channels; in both cases, the wave-1 anomaly starts at low latitudes in the SH hemisphere and propagates poleward. However, wave-1 amplitudes are twice as strong for Isidis storms as for Acidalia storms, leading to stronger localized radiative forcing. The possible interpretation is that the dust reservoir drained during dust removal is more localized to Isidis and/or contains more available dust.

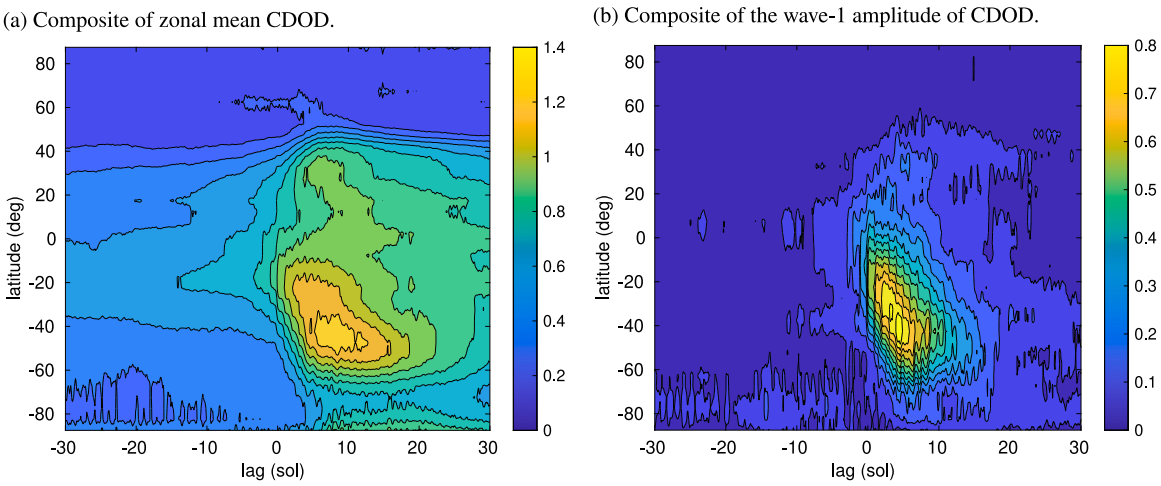



**Fig. 4.** Dust climatology surrounding regional storm onset red. Composites of all regional storms determined on Table 1 (i.e., including A and C season, Acidalia-type and Isidis-type regional storms).

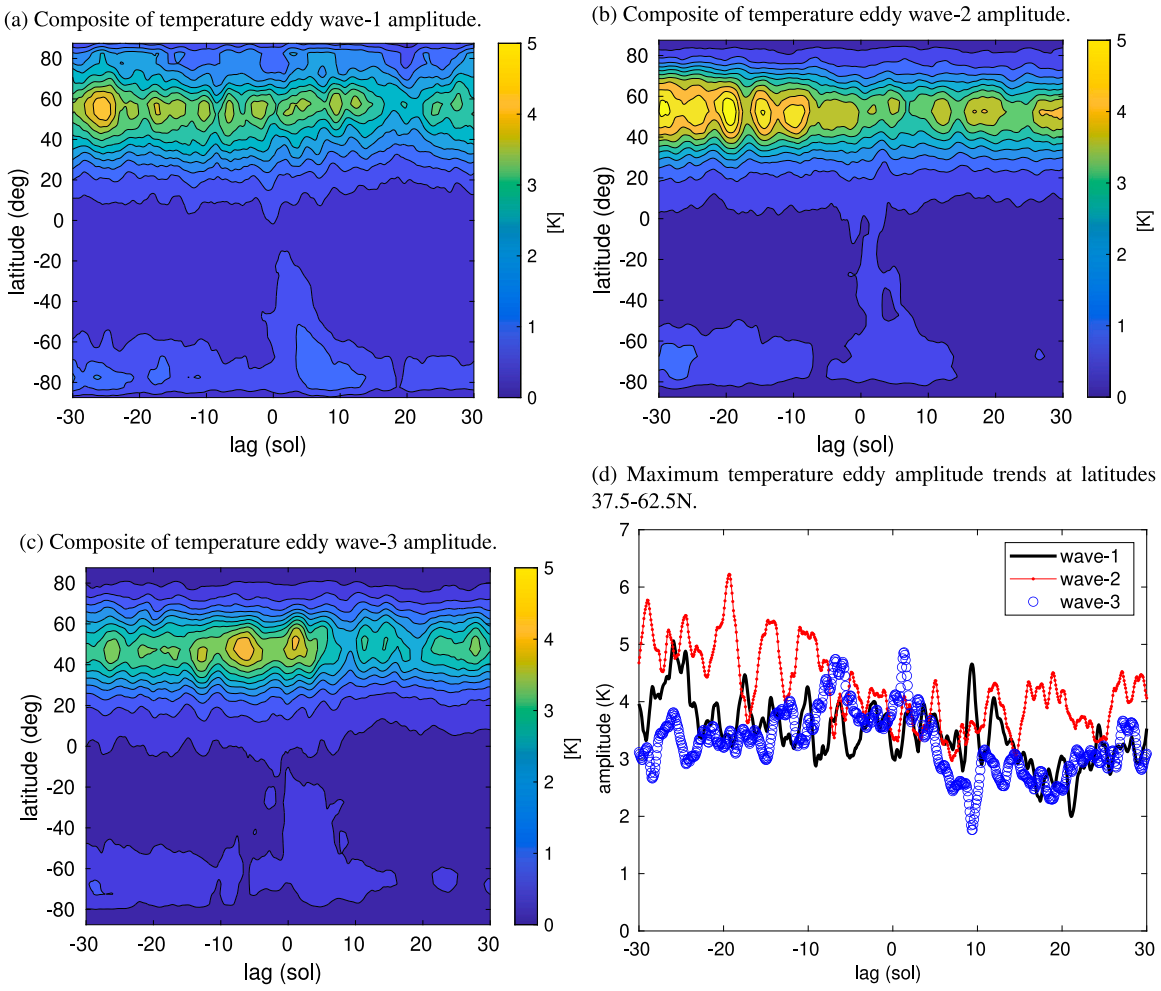



**Fig. 5.** Composite of temperature transient wave amplitudes at 1 km agl, wave-1 (a), wave-2 (b), wave-3 (c). Wave-1, 2, 3 eddy temperature trends, calculated as the maximum temperature eddy amplitudes in the composite between latitudes 37.5–62.5N, are summarized on panel (d). 2-sol running mean is applied for smoothing purposes on (a-c).

### *3.3.2. Dust storm propagation*

Here, we assess the evolution of the CDOD field, a few sols around the onset date. It is observed that the different Utopia–Isidis storms are quite similar spatially, and the Acidalia–Chryse storms possess more event-by-event variability. The composites of Isidis-type storms (Fig. 11) show a weak dust anomaly in the southwest corner of Isidis that starts approximately at sol −8 and slowly builds up to sol −1 when the dust is abruptly lifted from the surface. The equatorial easterlies then transport a portion of the locally lifted dust westward. The CDOD field also shows southward transport after onset. Once this transport

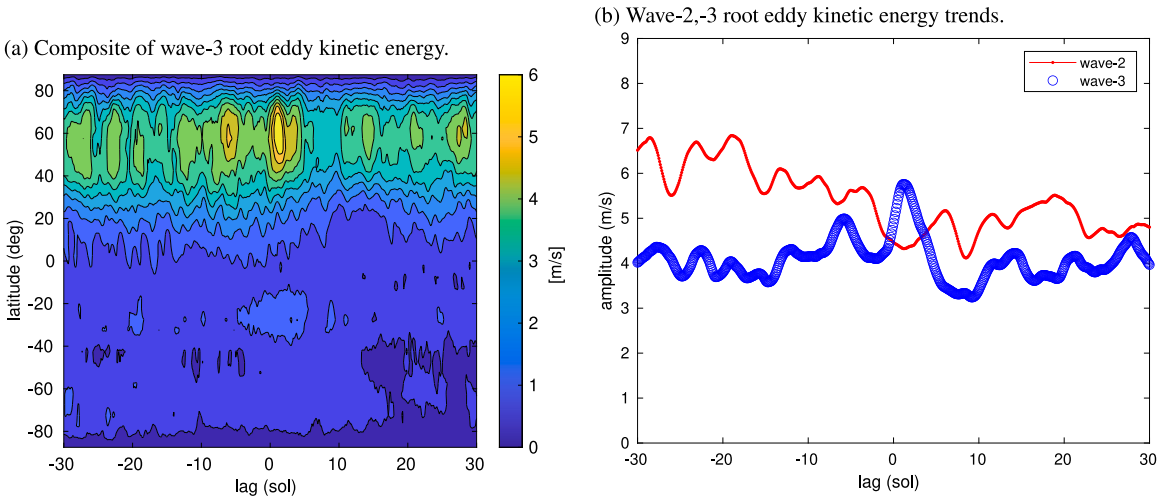



**Fig. 6.** Composite of wave-3 eddy kinetic energy at 1 km agl (a), and $\sqrt{EKE}$ wave-2,3 trends (b), that are calculated as the maximum $\sqrt{EKE}$ in the composite between latitudes 37.5–62.5N.

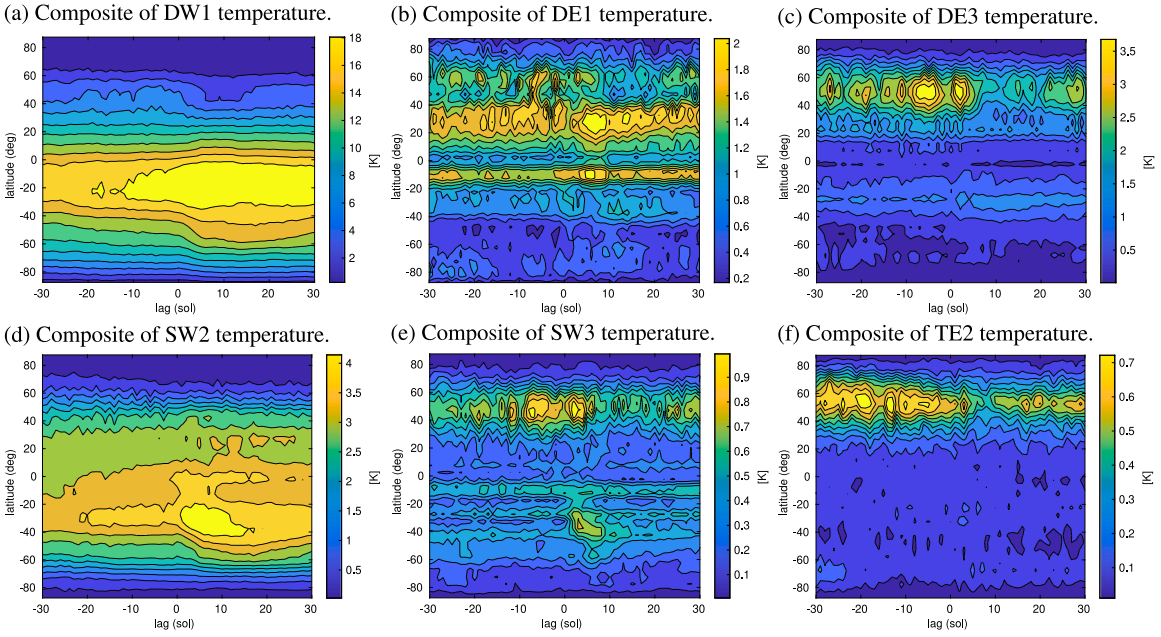



**Fig. 7.** Composite of the amplitude of temperature tide modes DW1 (a), DE1 (b), DE3 (c), SW2 (d), SW3 (e), TE2 (f) at 1 km agl.

reaches the SH mid-latitudes, the westerlies begin transporting dust to the east. Different Isidis storms share substantial similarities in these evolutionary traits, resulting in strong signatures in composite evolution.

Contrary to the rigidity of the Isidis storms, the Acidalia storms express more spatial variability (Fig. 12). The initiation of the local dust lifting takes place on a similar time scale as Isidis storms, starting around sol −8, and the lifted dust at sol 0 is then advected in a few possible directions. Although the overall dust content of the atmosphere is stronger than that of the Isidis storms, this variability results in weaker spatial signatures in the distribution of dust after onset.

### 3.3.3. Transient wave differences

The storm composites passing through the two different lowland channels reveal notable differences in transient wave precursors and impacts and, somewhat surprisingly, different signatures in the temperature (Fig. 13) and the v field composites (Fig. 14). Although the temperature wave-2 composites do not reveal any signature predictors, with the composite evolution showing a seasonal decay throughout the time window, the wave-2 v field exhibits notable features. First, it weakens significantly before onset, between sol −10 and 0 in the Acidalia composite. After onset, it recovers partially, although it remains weaker than before sol −10. Second, the Isidis composites exhibit several peaks before the onset and a weakening after the onset. Since the peak at sol −20 does not result in a regional storm within a few sols, it is unclear whether either that peak or the peak at sol −5 is a precursor of the regional storm or just part of natural variability. However, we appreciate that the wave-2 component of the v field might indicate the onset of an Isidis-type regional storm, and future Isidis events will likely provide more insight. In fact, Hinson and Wilson (2021) has pointed out that several early (i.e., pre-$L_s$ = 220°) regional storms were preceded by wave-2 activity, including MYs 26, 31, 33, with the MY 31 event preceded by a wave-2 event approximately 20 sols prior.

The wave-3 composites show the previously observed behavior for Isidis storms both in temperature and meridional wind, a peak at sol −8 and sol 1, with the peak in the temperature composite stronger at sol −8 and the peak in the meridional wind/EKE similar in magnitude at sol 1. The Acidalia composites show more variability. The temperature and

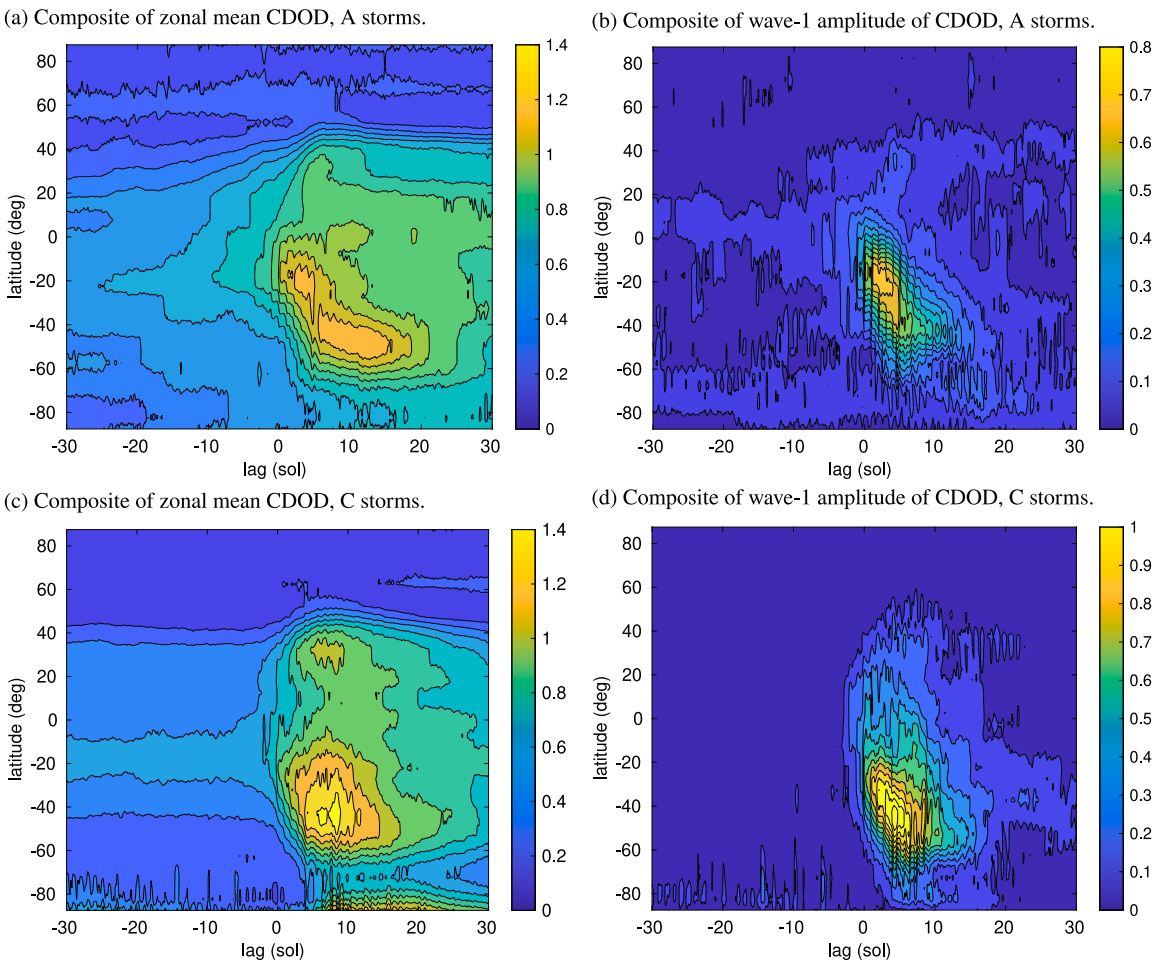



**Fig. 8.** Composites of CDOD surrounding regional storm onsets, A-season regional storms (a, b), C-season regional storms (c, d), zonal mean (a, c), wave-1 amplitude (b, d).

the v field composite exhibit multiple peaks before onset, particularly at sol −12 and sol −8. Inspecting Acidalia events case-by-case, we see that the wave-3 event at sol −12 is consistently present. However, it is not anomalously strong at certain events. Furthermore, Acidalia-type regional storms are preceded by multiple wave-3 events. Interestingly, these wave-3 events precede low-latitude increases in CDOD by a few sols (Fig. 10). Although we cannot directly link these two features, Acidalia A-storms may require multiple wave-3 events that gradually increase background dust levels before eventually manifesting in a regional storm. Such multiple wave-3 events preceding the regional storm have been noted for the Acidalia A-storms of MY 24 (Wang, 2018) and MY 27 (Hinson and Wang, 2010; Wang and Richardson, 2015).

### 3.3.4. *Differences in tides*

We find that, apart from TP3 for zonal wavenumber-3 modes, there is no noticeable difference between Acidalia and Isidis storms. We found no notable differences between the two channels for tide modes with zonal wavenumbers 1 and 2. Although zonal wave-3 tide anomalies are present for both Isidis and Acidalia, we find that they are a more consistent predictor of Isidis storms (for DE3, see Fig. 15), and similarly to transient waves, we find that multiple peaks precede Acidalia events.

### 3.3.5. *Tidal gate analysis*

To further elucidate potential tide-transient wave interactions, we extend our analysis to include a treatment of 'tidal gate' theory (Wang et al., 2003) using a composite analysis. The theory posits that a dust storm sequence can flush from NH mid-latitudes southward and cross the equator when the mid-latitude transient waves and low-latitude thermal tides align (i.e., the meridional components are southward), resulting in an approximately 10-hour time window each day when the mid-latitude transient waves can guide frontal storms towards 30–40N where tides can take over dust transport.

First, we adjust the onset dates of each regional storm so that each Acidalia storm onset occurs at 1:00 pm local time at longitude 50W, and each Isidis storm onset takes place at 2:40 pm local time at longitude 95E. This adjustment results in the phases of the tides being aligned simultaneously for the different events, allowing us to display tides in composites. The tidal gate is open between local times 1:00 pm and 11:00 pm for Acidalia, and 2:40 pm and 0:40 am for Isidis, i.e., the low-latitude tides (of the meridional wind) are consistently southward during these hours at 50W and 95E, respectively. Hence, we restrict our attention to these hours at each sol, and we consider the composite of the meridional velocity field comprising (i.e., the summation) of both tides and transient waves at longitudes 95E and 50 W for Isidis and Acidalia, respectively (Fig. 16).

Transient waves dominate the meridional winds poleward of 30N, tides dominate and are negative (southward) equatorward. Surprisingly, we see more phase locking between low-latitude tides and mid-latitude transient waves in the Isidis composites. Isidis storms are preceded by a strong mid-latitude signature of tidal gate interaction, especially at sol −8 and −6 when the meridional velocity field supports strong equatorward transport in the entirety of the 10-hour time window between 60N and the equator. The 30N v field is much stronger in the composite at these sols than is typical. Inspecting individual Isidis

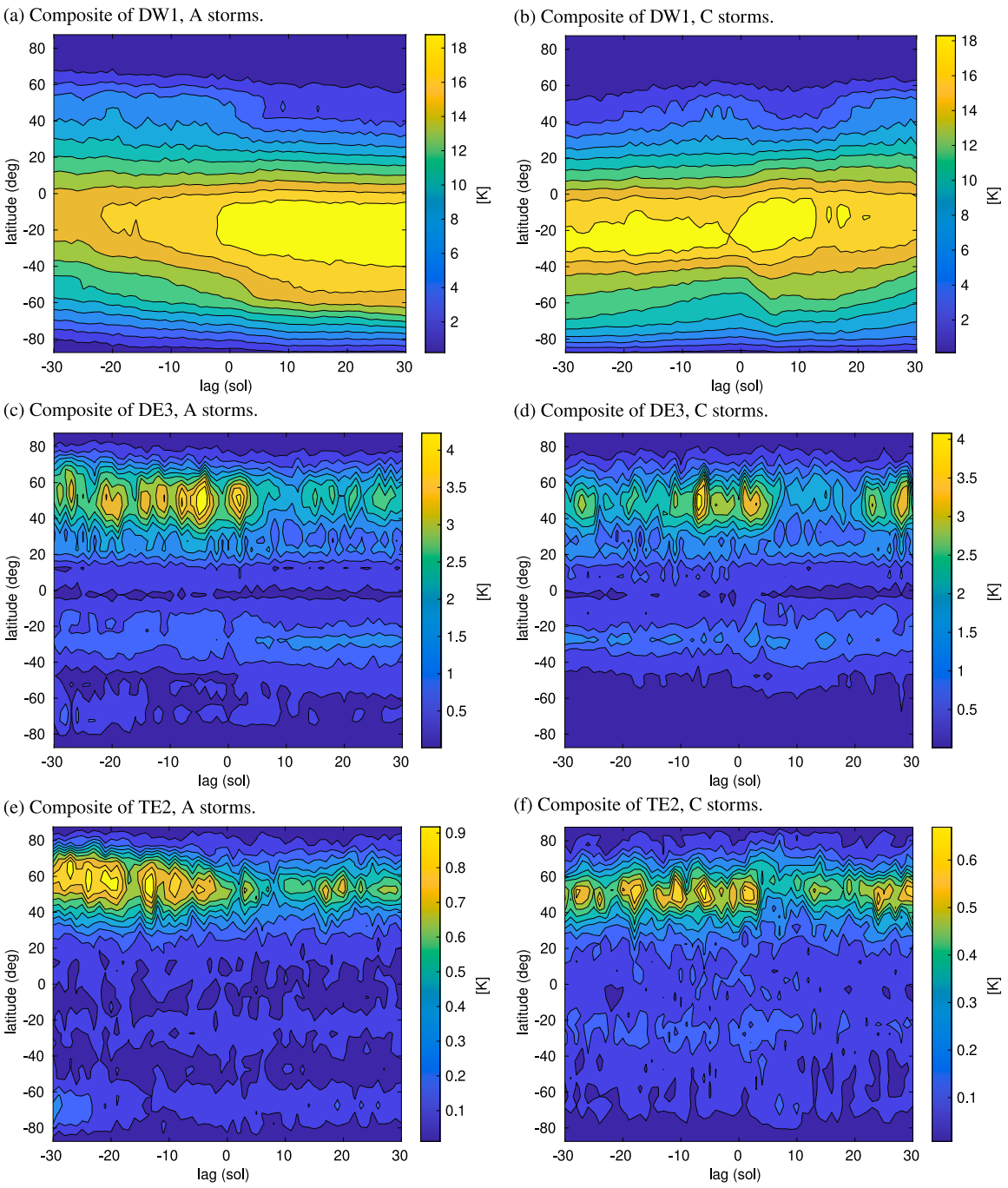



**Fig. 9.** Composites of the amplitude of DW1 temperature tide modes (a, b), DE3 temperature tides (c, d) and TE2 modes (e, f), A storms (a, c, e), C storms (b, d, f).

events, we find that all four events had a strong tide-transient phase locking at sols −8 and −6, showing that southward meridional transient waves preceded all Isidis events during the open tidal gate hours.

Although the Acidalia storm composite also exhibits tidal gate signatures, including at sols −11, −8, and −6, we find that it is not as consistent and strong across events as Isidis storms; therefore, here it is concluded that the tidal gate signature is stronger for Isidis than for Acidalia. This also adds to the perceived difference in variability of the two types of storms, as Isidis storms are more focused, and Acidalia requires more preconditioning.

### 3.4. Brief comparison with EMARS

While we are not aiming to provide a comparative study between multiple reanalysis datasets, we consider EMARS output here to discuss and validate key results that we derived from OpenMARS data.

#### 3.4.1. Differences in CDOD

The dust evolutions in both reanalysis data are based on Montabone et al. (2015). However, we notice that there are some differences in how the two reanalysis products determine output CDOD. Our regional storm onset definition determined the same date for most storms; however, in EMARS our definition was not met during the 29 C season, and in EMARS the onset date conditions were satisfied later in 30 A, at $L_s = 240°$ instead of $L_s = 232°$.

Since EMARS is only available until MY 32, we cannot comment on the dust storm initiation during MY 33 A; however, it is possible to compare it with the MY 32 A-season storm initiation. Similarly to

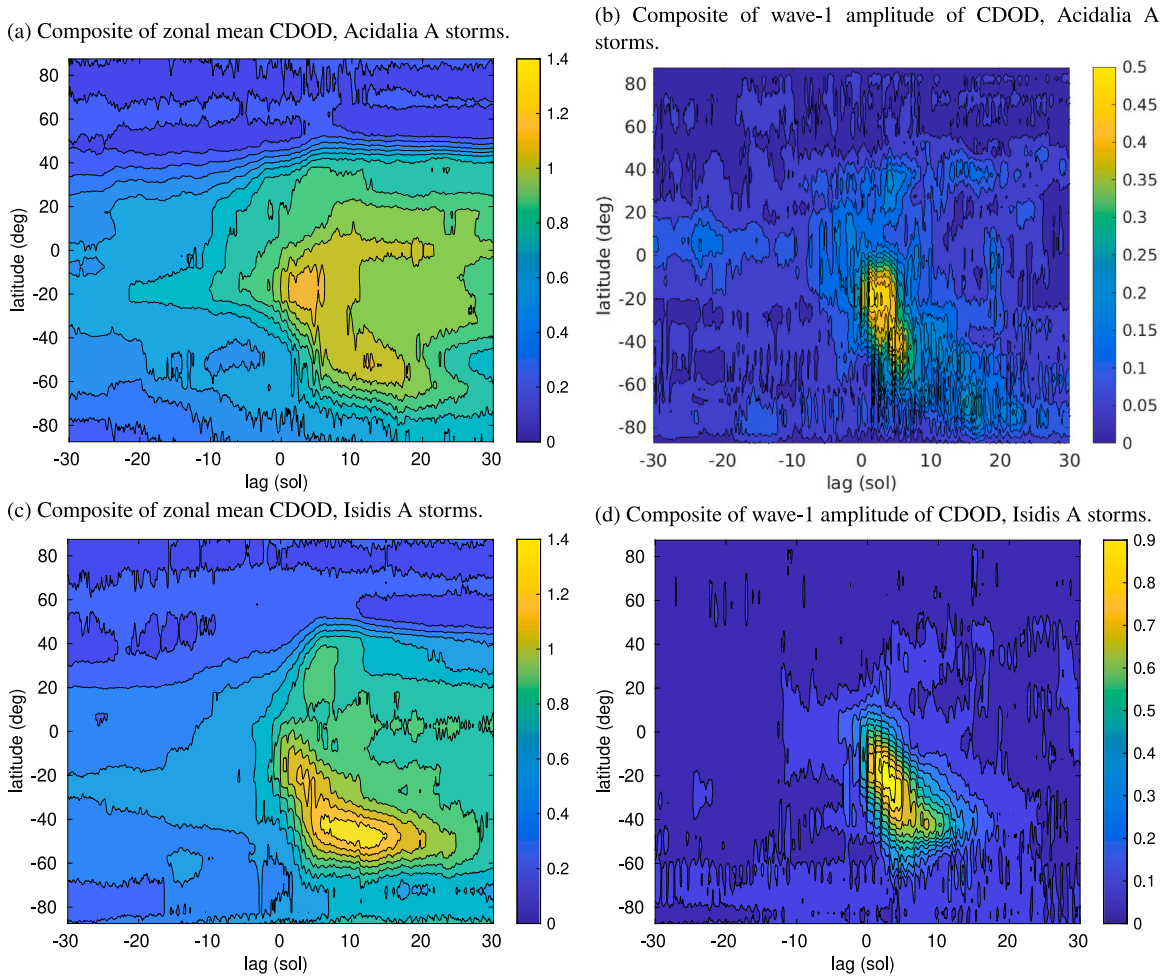



**Fig. 10.** Composites of CDOD surrounding regional storm onsets, Acidalia A-season regional storms (a, b), Isidis A-season regional storms (c, d), zonal mean (a, c), wave-1 amplitude (b, d).

OpenMARS, EMARS also produces dust opacities that originate at and west of Isidis, with the initial dust lifting taking place between Isidis and Hellas. The storm then spreads to the west, where it is enhanced by a local storm in Acidalia. Therefore, both the OpenMARS and EMARS assimilation schemes suggest that the MY 32 A-season regional storm was not initiated by Acidalia flushing. Instead, dust anomalies at Isidis seem to precede onset.

### 3.4.2. Wave-2,3 transient wave anomalies

Looking at the temperature composites of the EMARS data, we see that storm onsets are also preceded by a mid-latitude wave-3 pulse, so the signature is consistent across the reanalysis datasets (Fig. 17), although the amplitudes of these waves are weaker in EMARS than in OpenMars. However, the wave-2 amplitude in the meridional wind is less pronounced in EMARS. Although there is arguably a local maximum of 8 sols before onset, it is much weaker than the pulse around sol −20. Whether a peak in wave-2 is a predictor of the Isidis storm or is simply a result of variability requires more observations or modeling work.

### 3.4.3. Tidal precursors

Similarly to OpenMARS, EMARS also exhibits tide composites with mid-latitude NH tides stronger before onset and weaker after. However, no clear peak (dominated by Isidis events) is observed in the OpenMARS data. Looking at individual events, it is still possible to see strong tides at NH mid-latitudes (see Fig. 17 for DE3). However, they are less anomalous than in OpenMARS. Ultimately, based on EMARS tides, it would be hard to argue that high wave-3 tide amplitudes are precursors. According to EMARS, it is still possible that a stronger-than-seasonal tide component is present in the sols preceding regional storm onset.

## 3.5. Surface stress composites

Since surface stresses are one of the key contributors to dust lifting from the surface, next we use EMARS data to elucidate high surface stress regions and timings surrounding regional storm onset dates. Specifically, we capture anomalies in surface stresses by normalizing at each longitude-latitude grid point by the mean and standard deviation obtained from the time window between sol −30 and sol −4. We use the obtained surface stress anomalies to detect high surface stress regions between sols −2 and 2, distinguishing between Acidalia A storms and Isidis A storms by averaging over the 5-sol period across the different regional storm events. We find that the surface stresses for the Isidis storms, centered on Syrtis Major, are less variable than for the Acidalia storms, with the strongest signature at Solis Planum (Fig. 18), with the high-stress anomaly regions being more localized, resulting in a composite with higher anomalies in a more constrained region. Furthermore, at each latitude and time we consider the maximum surface stress anomaly (across all longitudes), and we construct a latitude-lag composite (Fig. 19).

We determined a high surface stress anomaly at 0–5 sols between the equator and 15S for Isidis A-storms. Surface stress anomalies then appear between 20S and 60S propagating polewards within the next

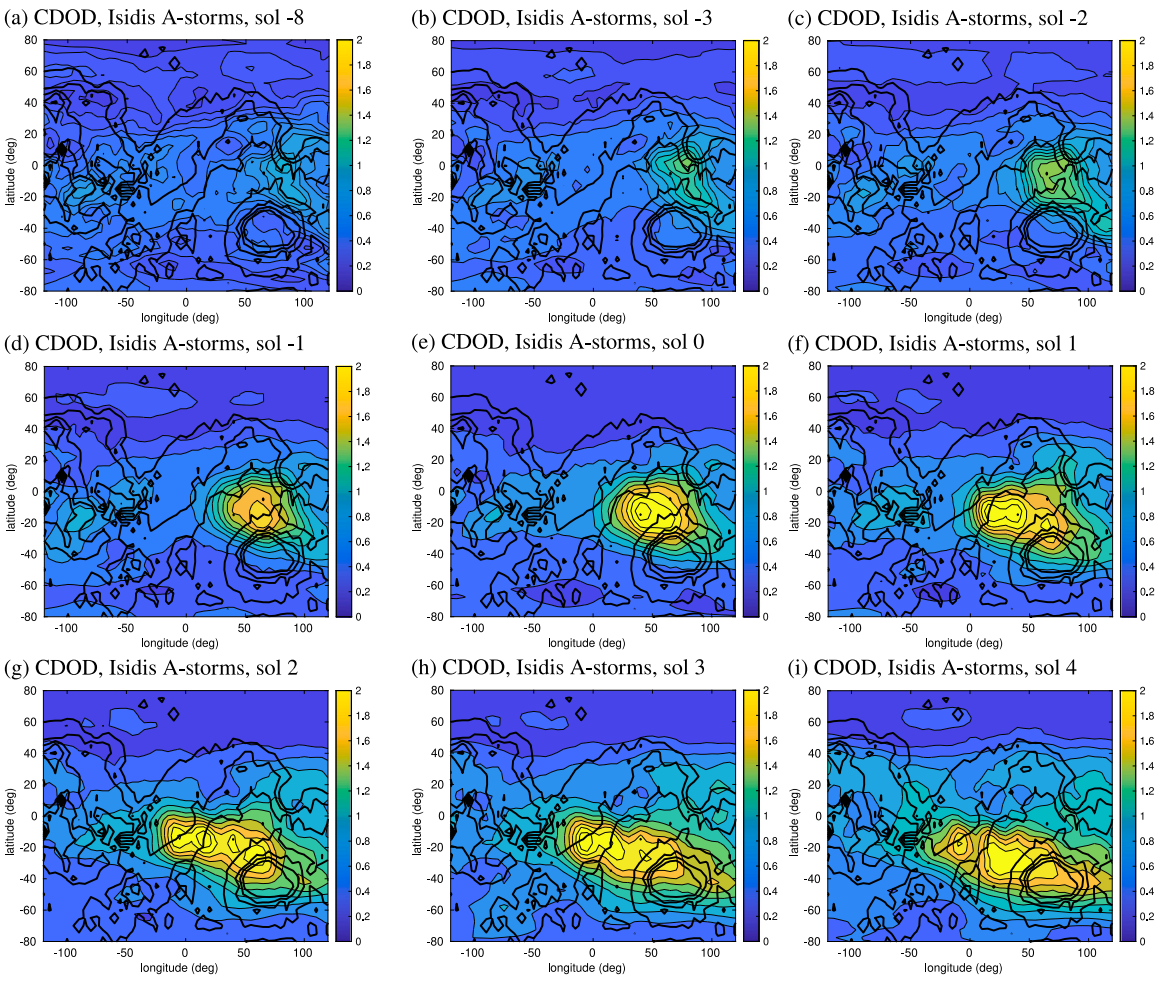



**Fig. 11.** Composite of CDOD evolution during Utopia–Isidis storms. Panels show the composite at sol −8 (a), and then sol −3 to sol 4 (b, c, d, e, f, g, h, i).

few sols. Furthermore, the 0–30S band exhibits high surface stresses after the onset at all times. On the other hand, Acidalia A-storms are accompanied by high surface stresses in a wider 0–40S latitude band, with maximum anomalies developing around 40S a few sols after onset. Hence, surface stresses within a few sols of onset are more focussed both spatially and temporally in the case of Isidis A-storms, compared to Acidalia A-storms. Both types of storms resulted in high surface stresses at the edge of the southern hemisphere polar ice cap.

## 4. Discussion

### *4.1. Regional storm onset definition and categorizations*

This study utilized reanalysis data (mainly OpenMARS) to conduct a composite analysis of regional dust storms in the A and C seasons. Our proposed 'regional storm onset date' is objectively defined, with the aim that while it is based on intuition, it can be calculated straightforwardly from the CDOD field. Our definition has potential applicability in long GCM runs aimed at assessing regional storm climatology. One weakness of our definition is that threshold values depend on the current season. While an onset date can be determined once the season has passed, it might not be a suitable metric for determining the onset date in real-time on the sol when it occurs. Although our definition may not be optimal, it would help identify predictors in future works on flushing storms if onset dates were determined through a similar objective definition rather than by visual inspection.

A further storm identification issue we experienced was the case of MY 32 and 33 A-season regional storms, both of which were previously classified as at least partly Acidalia-initiated storms (Wang et al., 2023). MCS opacity observations show weak signals from Isidis and MARCI imagery is more suggestive of influence from Acidalia (Wang et al., 2023). However, the evolution of reconstructed dust opacity support the idea that the dust lifting originated at Isidis instead of Acidalia. Although we are open to alternate classifications, both OpenMARS and EMARS CDOD output suggest that these storms were initiated at Isidis. Furthermore, surface stresses from EMARS also point towards the region west of Isidis where the initial dust lifting took place. Nonetheless, given the noted discrepancy between MARCI imagery and Montabone's dust reconstructions, we would encourage a comparative study between the two, to determine how reliable these sources are during dust storms.

Furthermore, we have found that regional storms exhibit significantly greater variability than previously reported in the literature. Only about half of the A-season storms are triggered by flushing through Acidalia. These regional storms seem to require preconditioning, i.e. multiple flushing events increase dust levels by the time the regional storm eventually occurs. In contrast, other regional storms originate in the Hellas–Syrtis–Isidis region, and the CDOD fields suggest initiation through Isidis. These events occur much faster than Acidalia events and appear to require little to no preconditioning. Since it was not clear in the images that Utopia flushing did precede these events in MY 32 and 33 (Wang et al., 2023) a few sols earlier, these storms may be, in fact, not preceded by visible frontal dust storms a few sols earlier, but by strong and localized surface stresses. All the slight details regarding individual events suggest that while there are shared similarities between different regional storm onset scenarios,

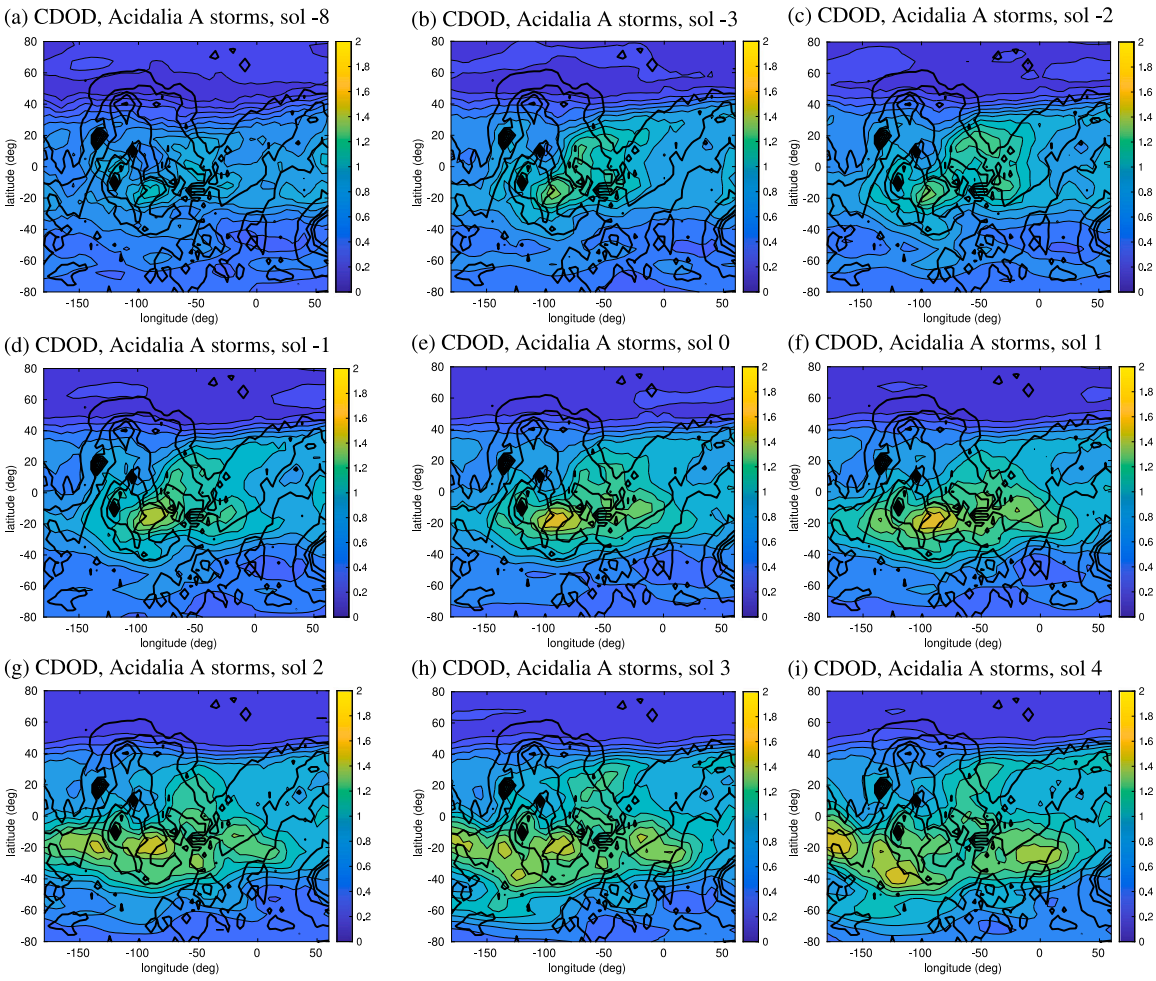



**Fig. 12.** Composite of CDOD evolution during Acidalia–Chryse A-season regional storms. Panels show the composite at sol −8 (a), and then sol −3 to sol 4 (b, c, d, e, f, g, h, i).

classifications by 'flushing channels' are more delicate than previously perceived.

#### 4.1.1. OpenMARS reliability

Our comparison of OpenMARS transient temperature waves with MCS brightness temperatures revealed that OpenMARS may not be reliable in capturing transient waves in the solstice season and strong agreement between the two datasets occur only until $L_s = 220° - 240°$. In the C-season, it cannot be clearly stated when the wave-1 and wave-2 transient waves become well-captured again by OpenMARS, but it is possible that not until $L_s = 340°$. However, the wave-3 amplitudes are seemingly well-captured as early as $L_s = 300°$. Therefore, based on the comparison, our results are the most reliable during early (i.e., Isidis-type) A-season regional storms. On the other hand, wave-1 and wave-2 precursors of C-season regional storms might be OpenMARS artifacts.

### 4.2. Precursors and impacts of regional storms

Our composite analysis has identified both the precursors and typical impacts of regional storms, as well as shared properties and differences between A- and C-season storms, and Acidalia and Isidis-type storms.

#### 4.2.1. Precursors

As previously observed for individual events (e.g. Hinson and Wang, 2010; Wang et al., 2005; Wang, 2018; Hinson and Wilson, 2021), the wave-3 transient wave is a consistent precursor for regional storms of any type (A or C, Acidalia, or Isidis), the temperature field in particular. Although the wave-3 transient wave in the meridional wind or EKE is also peaking approximately 8 sols before onset, it is less anomalous than the temperature spike. In contrast to this, the wave-2 meridional wind field is seemingly a predictor of Isidis storms, although the peak observed at sol −6 is not stronger than the peaks at sol −20. Therefore, a strong wave-2 might be necessary a few sols prior onset, but it might not be sufficient. In fact, the peak in wave-2 temperature amplitude 20 sols before onset presents the strongest wave-2 signal and could be itself a predictor of upcoming Isidis storms, complementing the results of Hinson and Wilson (2021). We have also found a universal strengthening in the temperature tides 8 sols before onset, and this anomaly is stronger than the seasonal variation. Either the tides and transient waves may interact to amplify each other (through, e.g., resonance), or the period of the transient waves shortens and is misclassified as tides, although transient waves typically have periods longer than 2 sols, so misclassification of transient waves as tides seems unlikely. It is also possible that these tides are OpenMARS artifacts, as EMARS did not exhibit anomalous tide amplification prior to regional storm onset.

#### 4.2.2. Impacts

Although the predictors are constrained to NH mid-latitudes around 8 sols before onset, we have determined impacts at both hemispheres and at a wider range of sols. We identified universally weak wave-3 transient temperature eddies and weak tides for all wavenumbers at NH mid-latitudes between sol 0 and 10. There is also a short-term strengthening of the SH tide lasting 15–20 sols, after which seasonality recovers. These hemispheric impacts on transient waves and tides result in a global decrease in EKE and a global increase in the kinetic energy

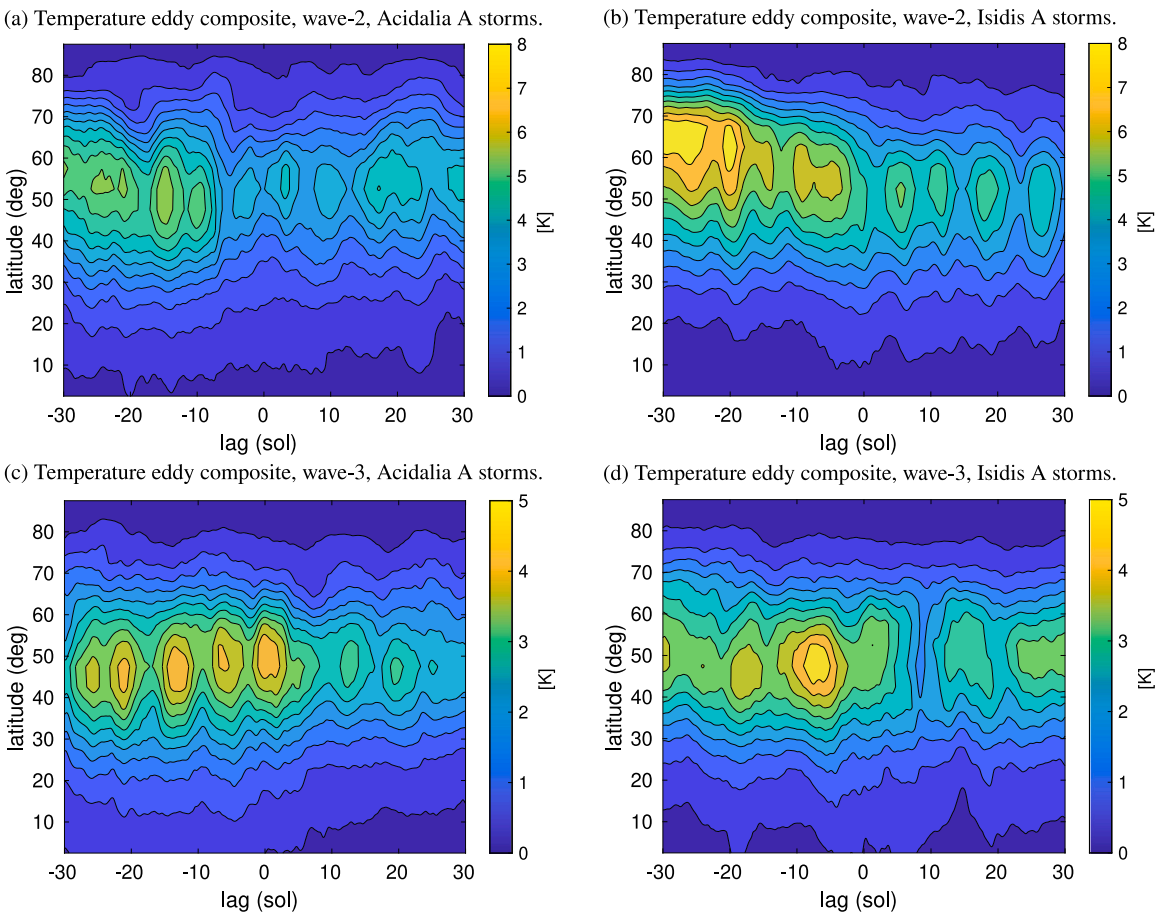



**Fig. 13.** Composites of temperature eddies surrounding regional storm onsets, Acidalia A-storms (a, c), Isidis A storms (b, d), wave-2 amplitude (a, b), wave-3 amplitude (c, d). 5-sol running mean is applied for smoothing purposes.

of the tide, which complements the results of Battalio and Wang (2020) in deriving these global trends. Interestingly, the evolution of the zonal CDOD expressed significant differences between regional storms of the A- and C-season and between Acidalia and Isidis storms.

#### 4.2.3. A- and C-season differences

We found little difference in the precursors of transient waves and the non-seasonal evolution of tides when comparing storms of the A and C seasons, with both types typically preceded by wave-3 transient wave activity and an increase in tides at mid-latitudes in the NH. However, the CDOD distribution is different both before and after onset. A-season storms (especially Acidalia storms) can be preceded by a sequence of storm events in which the low latitudes gradually become dusty. This is not present in the C-storm composite. Moreover, A-storm wave-1 CDOD composite shows a wave-1 anomaly propagating from the equator towards 60S after onset, whereas C-storms are seemingly initiated by a wave-1 anomaly between 40S–60S. After onset, the wave-1 anomaly has lived much longer for the C storm, which is indicative of a storm that is more longitudinally constrained, as has been observed for individual events (e.g. MY35-C, Martín-Rubio et al., 2024).

#### 4.2.4. Acidalia and Isidis differences

Acidalia storms experience more variability than Isidis storms. The spatiotemporal evolution of CDOD during Isidis storms is quite consistent across different events, however Acidalia events can be followed by the dust storm spreading to a number of different directions, also observed for the dust seasons of MYs 24–31 by Battalio and Wang (2021).

For both transient waves and tides, we found that the wave-3 amplitude at mid-latitude is a stronger precursor of Isidis storms than of Acidalia (although still present for Acidalia). The meridional wind composite also shows a high-amplitude wave-2 preceding Utopia storms. However, it is unclear whether it is an actual precursor or a result of natural variability. Surprisingly, we also found that the tidal gate theory might be more relevant to Isidis than to Acidalia.

#### 4.2.5. Tide-transient wave interactions

As seen in the OpenMARS data, both tides and transient waves were amplified in the composite eight sols before onset. As mentioned, amplification of the tide can result from the miscategorization of transient waves when the running mean filter is applied. However, not just wave-3 tides were amplified, but a wide range of wavenumbers, suggesting that at least some part of the amplification is not simply miscategorization. In addition, tidal gate composites, in particular Isidis, show (Fig. 16) a meridional wind strengthening at a wide range of latitudes at certain sols (e.g. sol −8). Since tides are dominant southward of 40 °N and transients north of 40 °, it is suggestive that in OpenMARS, the tidal components are amplified. Moreover, the transient and tidal waves appear to be phase-locked, which could result in resonant effects that amplify the combined effect of the two waves.

### 4.3. GCM applicability

We have demonstrated how a composite analysis can capture the predictors and impacts of regional storms based on reanalysis data, which comprises a limited amount of observed and modeled regional storms. However, future GCM studies covering a large number of flushing-generated regional storms may compare the model output composites to reanalysis composites as a means of confirming how

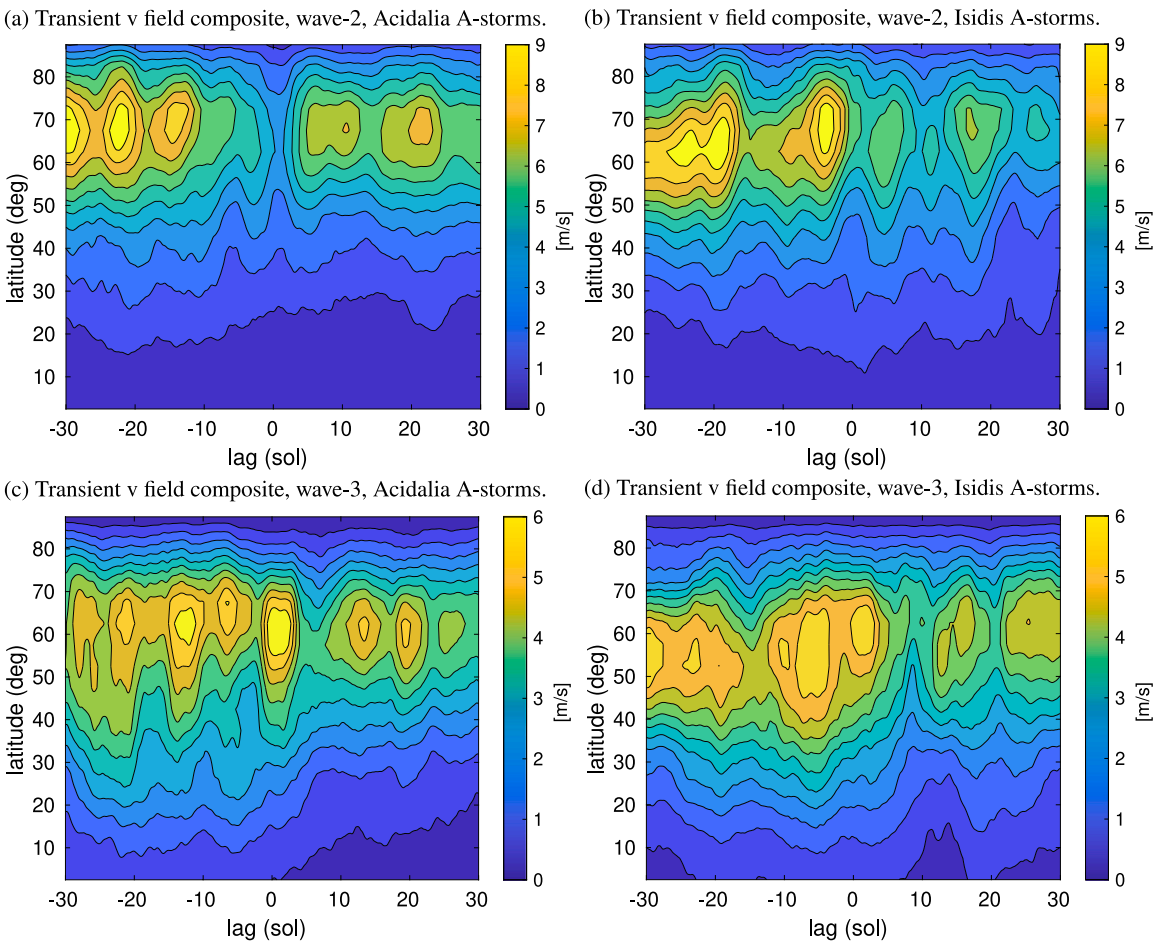



**Fig. 14.** Composites of transient v field amplitudes surrounding regional storm onsets, Acidalia A storms (a, c), Isidis A storms (b, d), wave-2 amplitude (a, b), wave-3 amplitude (c, d). 5-sol running mean is applied for smoothing purposes.

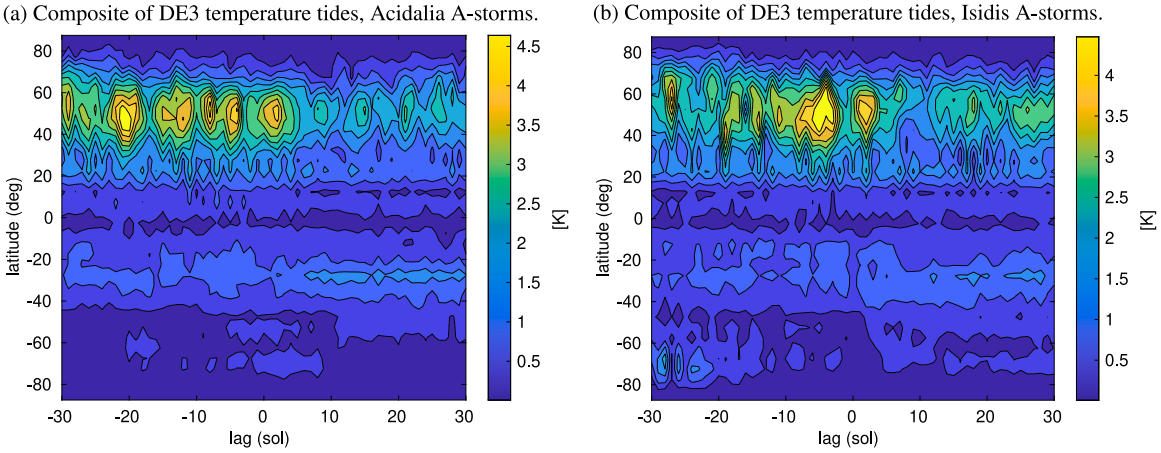


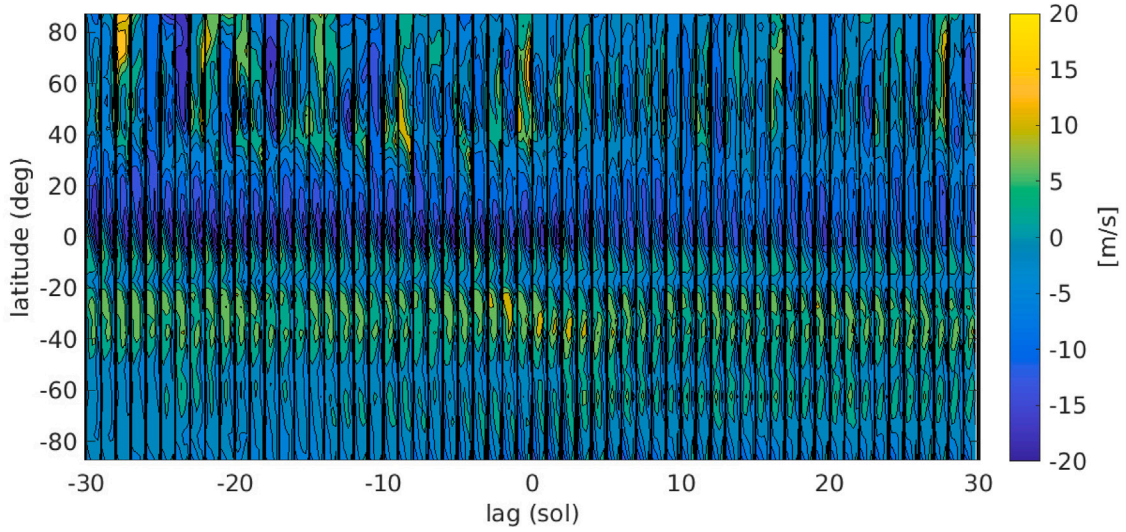

**Fig. 15.** Composite of DE3 temperature tides for Acidalia A-storms (a) and Utopia A-storms (b).

well model runs capture observation-based reanalysis predictors and impacts. Furthermore, a larger sample size provided by the GCMs could provide less noisy composites and a greater confidence in determining predictors and impacts. We believe that such studies seeking predictors should focus not only on transient wave precursors but also on potential tide amplifications and tidal gate analysis.

## 5. Conclusions

We used the composite analysis technique, based on reanalysis data, to determine the precursors and impacts of regional storms of the A and C seasons, and to identify similarities and differences between the A and C seasons and between regional storms of Acidalia and Isidis types.

(a) Composite of the aggregate tidal and transient meridional winds at 50W for Acidalia A-storms.




(b) Composite of the aggregate tidal and transient meridional winds at 95E for Isidis A-storms.

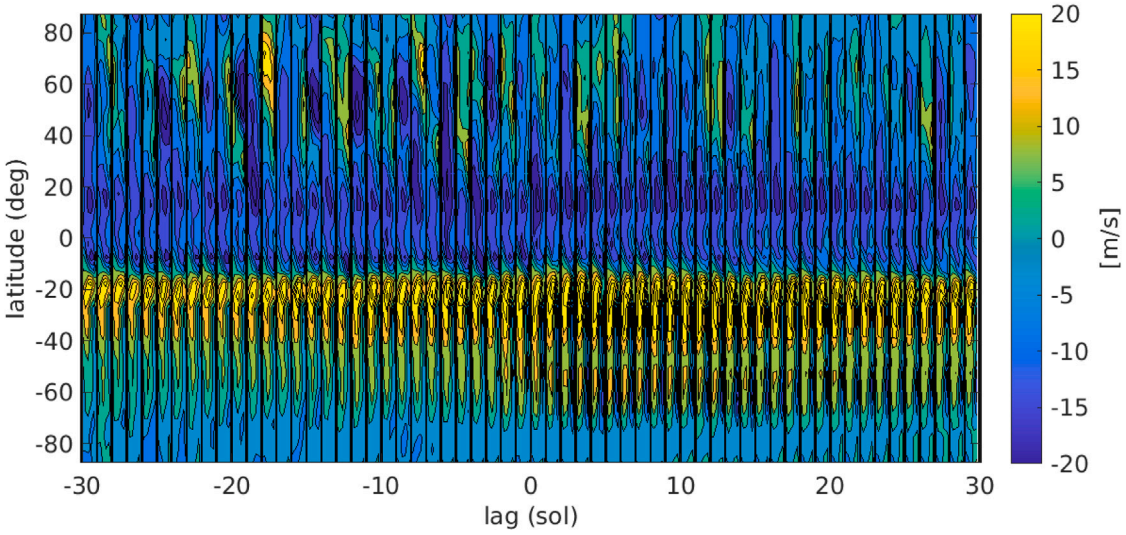
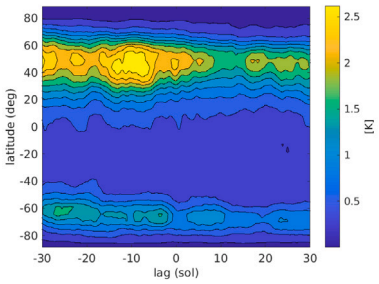
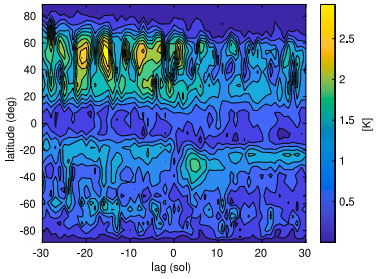



**Fig. 16.** Composite of the 1 km agl meridional wind comprising tides and transient waves at longitude 50 W for Acidalia storms (a) at 95E for Isidis storms (b), between approximately 1:00 pm/2:40 pm and 11:00 pm/0:40 am local time (Acidalia/Isidis, respectively). Black vertical lines separate subsequent sols for clarity.

(a) Composite of wave-3 temperature eddy amplitude, EMARS.




(b) Composite of DE3 amplitude, Utopia A-storms, EMARS.




(c) Composite of wave-2 meridional wind amplitude, EMARS.

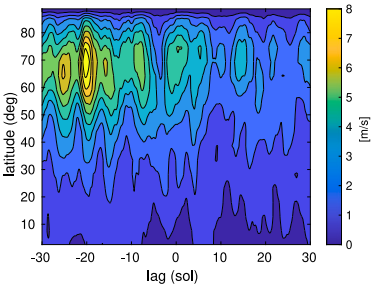



**Fig. 17.** Wave-3 transient wave amplitude (all storms) (a), DE3 temperature tide amplitude (Utopia A storms only) (b), and transient wave-2 meridional wind amplitude (Utopia A storms only) (c) composites in EMARS.

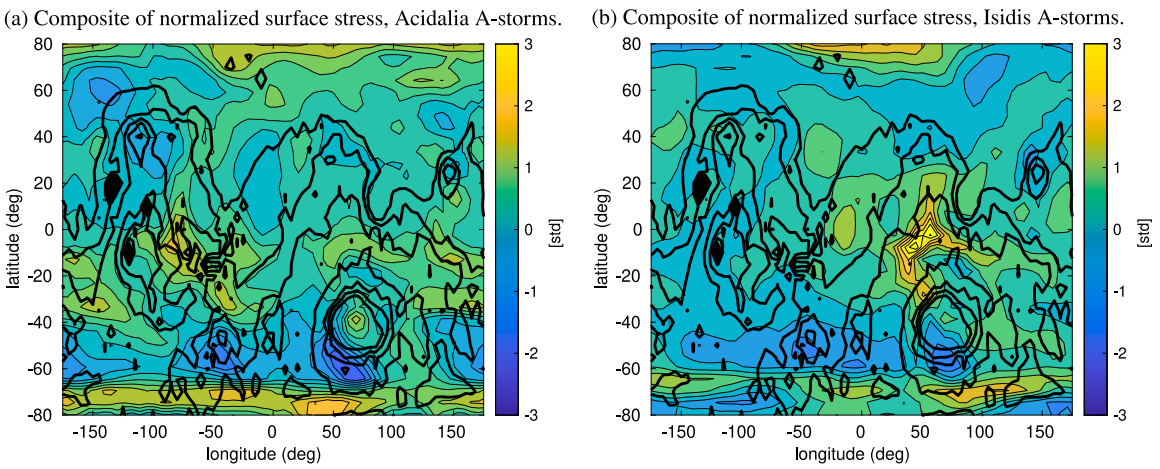



**Fig. 18.** Composites of normalized EMARS surface stress anomalies, averaged between sol −2 and 2, for Acidalia storms (a) and Isidis storms (b).

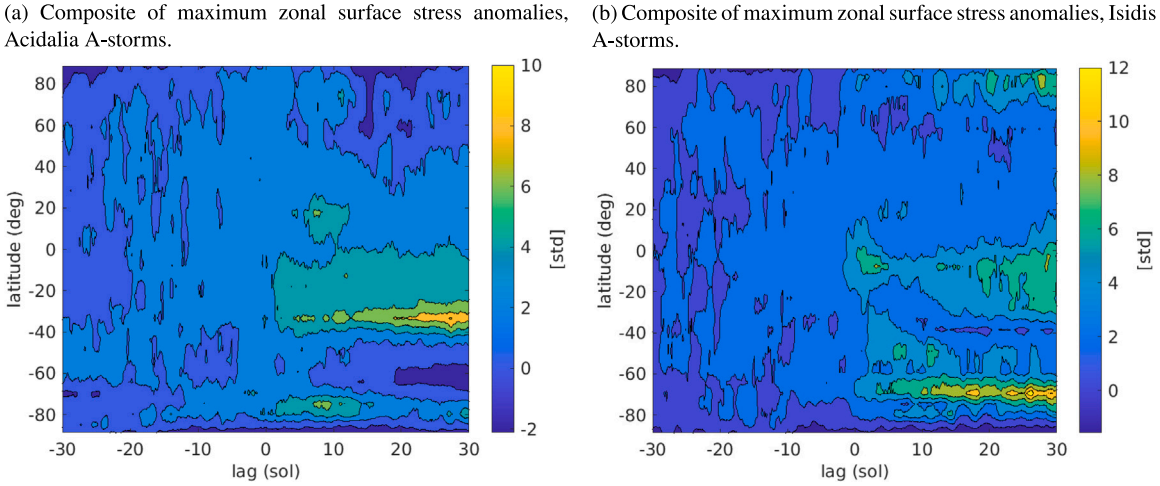



**Fig. 19.** Composites of normalized EMARS surface stress zonal maximum anomalies, for Acidalia A-storms (a) and Isidis A-storms (b).

In order to quantitatively compare different events, we have done and concluded the following:

1. Provided an objective definition of regional storm onset that was able to capture regional storms based on the timing of heavy dust lifting. Optimizing threshold values in the definition may be required if future events or MGCM output suggest that the values used here are too restrictive or permissive. Furthermore, the definition could be extended to distinguish objectively between different types (Acidalia, Hellas, Isidis) of regional storms.

Next, to distinguish between storms initiated at different spatial configurations, we inspected the evolution of the CDOD and identified that the spatial structure of regional storm initiation exhibits much more variability than previously reported in the literature. In particular,

2. The evolution of CDOD suggests Isidis-type storms in MY 32 and 33 A, however, MARCI images did not suggest immediate flushing activity through Isidis to Wang et al. (2023) a few sols preceding regional storm onset as potentially key images were not taken by MARCI at the right times to archive the Utopia/Isidis events. Hence, a Utopia/Isidis flushing sequence may or may not have occurred. Therefore, high surface stresses through Isidis may develop even without flushing storms, and this could trigger regional storms. For this reason, we refer to Utopia/Isidis-related regional storms as Isidis-type, rather than Utopia-type.

Given these classifications, we find that

3. Regional storms of the Isidis-type A season occur before $L_s = 220°$, whereas regional storms of the Acidalia-type A season occur after $L_s = 220°$. Although there is a seasonal change in the dominant component of baroclinic waves from wave-2 to wave-3 around $L_s = 220°$, Isidis-type storm composites still show wave-3 precursors in transient waves and tides. So, the dominance of wave-2 in the pre-$L_s = 220°$ season does not necessarily explain the seasonality between the Isidis and Acidalia storms. Alternatively, the seasonality of the Isidis and Acidalia-initiated regional storms may be linked to the phase of the NH forced wave 1 wave (not discussed here), which undergoes a phase change around $L_s = 225°$ (Hinson and Wilson, 2024).

Using the proposed definition of the onset and spatial categorization, we determined the following precursors and impacts.

4. Regional storms are typically preceded by an amplification of the wave-3 baroclinic wave at NH mid-latitudes 6–8 sols before onset and followed by a weakening 3–12 sols afterward. This result is consistent between the A and C seasons and between Acidalia- and Isidis-type storms, with some variability in timing. Isidis-type A season storms are preceded by a wave-2 amplification 20 sols prior onset.
5. A mid-latitude amplification of the tides is also apparent, most prominently of the modes with zonal wavenumbers 3 and 4,

between sol −6 and −4. This amplification is stronger in the A season than in the C season and is more localized in time for Isidis-type storms than for Acidalia-type storms.

6. Acidalia-type storms are preceded by higher atmospheric dust loading than Isidis-type storms, suggesting that a sequence of flushing storms may be required to precondition the atmosphere to gradually increase surface stresses to trigger an Acidalia-type regional storm, complementing the results of Wang (2018) (MY 24) and Hinson and Wang (2010), Wang and Richardson (2015) (MY 27). In contrast, Isidis-type storms do not require an increase in atmospheric dust and may occur more abruptly.
7. There are signals of a tide-transient wave phase locking that is more evident for Isidis-type storms and typically occurs 8 and 6 and 4 sols before onset. These timings align well with the amplification of baroclinic waves and tides, suggesting potential interactions between tides and transient waves.
8. The evolution of CDOD following the onset of regional dust storms is more variable for Acidalia-type storms and more spatially robust and potentially predictable for Isidis-type storms.
9. Isidis-type storms are characterized by strong, focused surface stress anomalies at Syrtis Major, and Acidalia-type storms are typically accompanied by surface stress anomalies at Solis Planum.
10. C-season storms require less preceding background dust than A-season storms. Post-onset, the zonal mean CDOD is more restricted to the SH mid-latitudes and of shorter duration for C-storms, and is transported to the north at a higher rate, lasting for a longer duration for A-season regional storms. The wave-1 component of CDOD peaks at higher SH latitudes and is stronger for C-season regional storms than for A-season storms, suggesting a more spatially localized type of event.

## CRediT authorship contribution statement

**Márton Mester:** Writing – original draft, Software, Methodology, Investigation, Formal analysis, Conceptualization. **R. John Wilson:** Writing – review & editing, Validation, Software, Methodology, Investigation, Conceptualization. **Melinda A. Kahre:** Writing – review & editing, Project administration, Funding acquisition.

## Declaration of competing interest

The authors declare that they have no known competing financial interests or personal relationships that could have appeared to influence the work reported in this paper.

## Acknowledgments

MM is funded by the NASA Postdoctoral Program. Support for this research was also provided by NASA's Planetary Science Division Research Program, through the Mars Climate Modeling Center (MCMC) Internal Scientist Funding Model (ISFM) work package at Ames Research Center. The authors would like to thank the three anonymous reviewers for their valuable comments and suggestions, which helped to improve the quality of this manuscript.

## Data availability

The OpenMARS reanalysis (version 5 used in this study) is freely available at Holmes et al. (2019). The EMARS reanalysis is freely available at Greybush et al. (2018) with descriptions provided at Greybush et al. (2019b).

## References

Alsaeed, N.R., Hayne, P.O., Concepcion, V., 2024. Seasonal and inter-annual variability in the polar vortex and snowfall on mars. J. Geophys. Res.: Planets 129, e2024JE008397. http://dx.doi.org/10.1029/2024JE008397.

Barnes, J., Haberle, R., Wilson, R., Lewis, S., Murphy, J., Read, P., 2017. The Atmosphere and Climate of Mars. Cambridge University Press, pp. 229–294, chapter The Global Circulation.

Barnes, J.R., Pollack, J.B., Haberle, R.M., Leovy, C.B., Zurek, R.W., Lee, H., Schaeffer, J., 1993. Mars atmospheric dynamics as simulated by the nasa ames general circulation model: 2. transient baroclinic eddies. J. Geophys. Res.: Planets 98, 3125–3148. http://dx.doi.org/10.1029/92JE02935.

Battalio, J.M., 2022. Transient eddy kinetic energetics on mars in three reanalysis datasets. J. the Atmospheric Sci. 79, 361–382. http://dx.doi.org/10.1175/JAS-D-21-0038.1.

Battalio, M.J., Lora, J.M., 2021. Annular modes of variability in the atmospheres of mars and titan. Nat. Astron. 5, 1139–1147. http://dx.doi.org/10.1038/s41550-021-01447-4.

Battalio, M., Wang, H., 2020. Eddy evolution during large dust storms. Icarus 338, 113507. http://dx.doi.org/10.1016/j.icarus.2019.113507.

Battalio, M., Wang, H., 2021. The mars dust activity database (mdad): A comprehensive statistical study of dust storm sequences. , Icarus 354, 114059, https://www.sciencedirect.com/science/article/pii/S001910352030405X, DOI: 10.1016/j.icarus.2020.114059.

Batterson, C.M., Kahre, M.A., Bridger, A.F., Wilson, R.J., Urata, R.A., Bertrand, T., 2023. Modeling the "b" regional dust storm on mars: Dust lofting mechanisms predicted by the new nasa ames mars gcm. , Icarus 400, 115542. http://dx.doi.org/10.1016/j.icarus.2023.115542, https://www.sciencedirect.com/science/article/pii/S0019103523001197.

Cantor, B.A., James, P.B., Caplinger, M., Wolff, M.J., 2001. Martian dust storms: 1999 mars orbiter camera observations. J. Geophys. Res.: Planets 106, 23653–23687. http://dx.doi.org/10.1029/2000JE001310.

Chree, C., 1913. Iii. some phenomena of sunspots and of terrestrial magnetism at kew observatory. Philosophical transactions of the royal society of London. Series a. Contain. Pap. A Math. Or Phys. Character 212, 75–116. http://dx.doi.org/10.1098/rsta.1913.0003.

Forbes, J.M., Bridger, A.F.C., Bougher, S.W., Hagan, M.E., Hollingsworth, J.L., Keating, G.M., Murphy, J., 2002. Nonmigrating tides in the thermosphere of mars. J. Geophys. Res.: Planets 107, 23–1–23–12. http://dx.doi.org/10.1029/2001JE001582.

Greybush, S.J., Gillespie, H.E., Wilson, R.J., 2019a. Transient eddies in the tes/mcs ensemble mars atmosphere reanalysis system (emars). Icarus 317, 158–181. http://dx.doi.org/10.1016/j.icarus.2018.07.001.

Greybush, S.J., Kalnay, E., Wilson, R.J., Hoffman, R.N., Nehrkorn, T., Leidner, M., Eluszkiewicz, J., Gillespie, H.E., Wespetal, M., Zhao, Y., Hoffman, M., Dudas, P., McConnochie, T., Kleinböhl, A., Kass, D., McCleese, D., Miyoshi, T., 2019b. The ensemble mars atmosphere reanalysis system (emars) version 1.0. Geosci. Data J. 6, 137–150. http://dx.doi.org/10.1002/gdj3.77.

Greybush, S.J., Kalnay, E., Wilson, R.J., Hoffman, R.N., Nehrkorn, T., Leidner, M., Eluszkiewicz, J., Gillespie, H.E., Wespetal, M., Zhao, Y., Hoffman, M., Dudas, P., McConnochie, T., Kleinböhl, A., McCleese, D.J., Miyoshi, T., 2018. The ensemble mars atmosphere reanalysis system (emars) version 1.0 dataset. http://dx.doi.org/10.18113/D3W375.

Hinson, D.P., Wang, H., 2010. Further observations of regional dust storms and baroclinic eddies in the northern hemisphere of mars. , Icarus 206, 290–305. http://dx.doi.org/10.1016/j.icarus.2009.08.019, https://www.sciencedirect.com/science/article/pii/S0019103509003613. solar Wind Interactions with Mars.

Hinson, D.P., Wilson, R.J., 2021. Baroclinic waves in the northern hemisphere of mars as observed by the mro mars climate sounder and the mgs thermal emission spectrometer. Icarus 357, 114152. http://dx.doi.org/10.1016/j.icarus.2020.114152.

Hinson, D., Wilson, J., 2024. Dust-storm forcing of rossby waves on mars. Icarus 412, 115998. http://dx.doi.org/10.1016/j.icarus.2024.115998, https://www.sciencedirect.com/science/article/pii/S0019103524000563.

Holmes, J., Lewis, S., Patel, M., 2019. Openmars database. http://dx.doi.org/10.21954/ou.rd.c.4278950, https://ordo.open.ac.uk/collections/OpenMARS_database/4278950.

Holmes, J.A., Lewis, S.R., Patel, M.R., 2020. Openmars: A global record of martian weather from 1999 to 2015. Planet. Space Sci. 188, 104962. http://dx.doi.org/10.1016/j.pss.2020.104962.

Kahre, M., Murphy, J., Newman, C., Wilson, R., Cantor, B., Lemmon, M., Wolff, M., 2017. The Atmosphere and Climate of Mars. Cambridge University Press, pp. 295–337, chapter The Mars dust cycle.

Kass, D.M., Kleinböhl, A., McCleese, D.J., Schofield, J.T., Smith, M.D., 2016. Interannual similarity in the martian atmosphere during the dust storm season. Geophys. Res. Lett. 43, 6111–6118. http://dx.doi.org/10.1002/2016GL068978.

Martin, L.J., Zurek, R.W., 1993. An analysis of the history of dust activity on mars. J. Geophys. Res.: Planets 98, 3221–3246. http://dx.doi.org/10.1029/92JE02937.

Martín-Rubio, C., Vicente-Retortillo, A., Gómez, F., Rodríguez-Manfredi, J., 2024. Interannual variability of regional dust storms between mars years 24 and 36. Icarus 412, 115982. http://dx.doi.org/10.1016/j.icarus.2024.115982.

Montabone, L., Forget, F., Millour, E., Wilson, R., Lewis, S., Cantor, B., Kass, D., Kleinböhl, A., Lemmon, M., Smith, M., Wolff, M., 2015. Eight-year climatology of dust optical depth on mars. Icarus 251, 65–95. http://dx.doi.org/10.1016/j.icarus.2014.12.034, ynamic Mars.

Montabone, L., Marsh, K., Lewis, S.R., Read, P.L., Smith, M.D., Holmes, J., Spiga, A., Lowe, D., Pamment, A., 2014. The mars analysis correction data assimilation (macda) dataset v1.0. Geosci. Data J 1, 129–139. http://dx.doi.org/10.1002/gdj3.13.

Storch, Zwiers, F.W., 1999. Statistical Analysis in Climate Research. Cambridge University Press.

Streeter, P., Lewis, S., Patel, M., Holmes, J., Rajendran, K., 2024a. An eight-year climatology of the martian northern polar vortex. Icarus 409, 115864. http://dx.doi.org/10.1016/j.icarus.2023.115864.

Streeter, P.M., Rajendran, K., Lewis, S.R., Olsen, K., Trokhimovskiy, A., Korablev, O., R, P.M, 2024b. Global heterogeneous chlorine chemistry: modelling and implications. In: The Tenth International Conference on Mars.

Taysum, B.M., Palmer, P.I., Olsen, K., Luginin, M., Ignatiev, N., Trokhimovskiy, A., Shakun, A., Grigoriev, A.V., Montmessin, F., Korablev, O., 2024. Observed seasonal changes in martian hydrogen chloride explained by heterogeneous chemistry. Astron. Astrophys. 687, A191. http://dx.doi.org/10.1051/0004-6361/202449546.

Wang, H., 2018. Cross-equatorial flushing dust storms and northern hemisphere transient eddies: An analysis for mars year 24. J. Geophys. Res.: Planets 123, 1732–1745. http://dx.doi.org/10.1029/2018JE005623.

Wang, H., Richardson, M.I., 2015. The origin. Evol. Trajectory Large Dust Storms Mars Dur. Mars Years 24– 30 ( 1999– 2011). Icarus 251, 112–127. http://dx.doi.org/10.1016/j.icarus.2013.10.033, dynamic Mars.

Wang, H., Richardson, M.I., Toigo, A.D., Newman, C.E., 2013. Zonal wavenumber three traveling waves in the northern hemisphere of mars simulated with a general circulation model. Icarus 223, 654–676. http://dx.doi.org/10.1016/j.icarus.2013.01.004.

Wang, H., Richardson, M.I., Toigo, A.D., Newman, C.E., 2024. Large scale oscillations in the martian tropical cloud belt. J. Geophys. Res.: Planets 129, e2024JE008479. http://dx.doi.org/10.1029/2024JE008479, 2024JE008479.

Wang, H., Richardson, M.I., Wilson, R.J., Ingersoll, A.P., Toigo, A.D., Zurek, R.W., 2003. Cyclones, tides, and the origin of a cross-equatorial dust storm on mars. Geophys. Res. Lett. 30, http://dx.doi.org/10.1029/2002GL016828.

Wang, H., Saidel, M., Richardson, M.I., Toigo, A.D., Battalio, J.M., 2023. Martian dust storm distribution and annual cycle from mars daily global map observations. Icarus 394, 115416. http://dx.doi.org/10.1016/j.icarus.2022.115416.

Wang, H., Zurek, R.W., Richardson, M.I., 2005. Relationship between frontal dust storms and transient eddy activity in the northern hemisphere of mars as observed by mars global surveyor. J. Geophys. Res.: Planets 110, http://dx.doi.org/10.1029/2005JE002423.

Wilson, R.J., 2012. Martian dust storms, thermal tides, and the hadley circulation. Comp. Clim. Terr. Planets https://www.lpi.usra.edu/meetings/climatology2012/pdf/8069.pdf.

Wilson, R.J., Hamilton, K., 1996. Comprehensive model simulation of thermal tides in the martian atmosphere. J. Atmospheric Sci. 53, 1290–1326. http://dx.doi.org/10.1175/1520-0469(1996)053<1290:CMSOTT>2.0.CO;2.

Zurek, R.W., 1976. Diurnal tide in the martian atmosphere. J. Atmospheric Sci. 33, 321–337. http://dx.doi.org/10.1175/1520-0469(1976)033<0321:DTITMA>2.0.CO;2.

Zurita-Zurita, S., Juárez, M. de la Torre, Newman, C.E., Viúdez-Moreiras, D., Kahanpää, H.T., Harri, A.M., Lemmon, M.T., a, J. Pla-García, Rodríguez-Manfredi, J.A., 2022. Mars surface pressure oscillations as precursors of large dust storms reaching gale. J. Geophys. Res.: Planets 127, e2021JE007005. http://dx.doi.org/10.1029/2021JE007005.